nature nanotechnology

SUPPLEMENTARY INFORMATION

https://doi.org/10.1038/s41565-020-0653-1

In the format provided by the authors and unedited.

Charge disproportionate molecular redox for discrete memristive and memcapacitive switching

In the format provided by the authors and unedited

nature nanotechnology

SUPPLEMENTARY INFORMATION

https://doi.org/10.1038/s41565-020-0653-1

In the format provided by the authors and unedited.

Charge disproportionate molecular redox for discrete memristive and memcapacitive switching

Sreetosh Goswami[1,2] ✉, Santi P. Rath[3], Damien Thompson[4] ✉, Svante Hedström[5,13], Meenakshi Annamalai[1], Rajib Pramanick[3], B. Robert Ilic[6], Soumya Sarkar[1,2], Sonu Hooda[1], Christian A. Nijhuis[1,7,8], Jens Martin[1,8,9,14] ✉, R. Stanley Williams[10], Sreebrata Goswami[3] ✉ and T. Venkatesan[1,2,9,11,12] ✉

[1]NUSNNI-NanoCore, National University of Singapore, Singapore, Singapore. [2]NUS Graduate School for Integrative Science and Engineering, National University of Singapore, Singapore, Singapore. [3]School of Chemical Sciences, Indian Association for the Cultivation of Science (IACS), Kolkata, India. [4]Department of Physics, Bernal Institute, University of Limerick, Limerick, Ireland. [5]Fysikum, Stockholm University, Stockholm, Sweden. [6]Center for Nanoscale Science and Technology, National Institute of Standards and Technology, Gaithersburg, MD, USA. [7]Department of Chemistry, National University of Singapore, Singapore, Singapore. [8]Centre for Advanced 2D Materials, National University of Singapore, Singapore, Singapore. [9]Department of Physics, National University of Singapore, Singapore, Singapore. [10]Department of Electrical and Computer Engineering, Texas A&M University, College Station, TX, USA. [11]Department of Electrical and Computer Engineering, National University of Singapore, Singapore, Singapore. [12]Materials Science and Engineering Department, National University of Singapore, Singapore, Singapore. [13]Present address: Svensk Kärnbränslehantering, Solna, Sweden. [14]Present address: Leibniz Institut für Kristallzüchtung, Materials Science Department, Berlin, Germany. ✉
e-mail: sreetosh@u.nus.edu; damien.thompson@ul.ie; jens.martin@ikz-berlin.de; icsg@iacs.res.in; Venky@nus.edu.sg

Supplementary Material for

Charge disproportionate molecular redox for discrete memristive and memcapacitive switching

Sreetosh Goswami[1,2*], Santi P. Rath[3], Damien Thompson[4*], Svante Hedström[5], Meenakshi Annamalai[1], Rajib Pramanick[3], B. Robert Ilic[6], Soumya Sarkar[1,2], Sonu Hooda[1], Christian A. Nijhuis[1,7,8], Jens Martin[1,8,9*], R. Stanley Williams[10], Sreebrata Goswami[3*] and T. Venkatesan[1,2,9,11,12*]

[1]NUSNNI-NanoCore, National University of Singapore, Singapore 117411

[2]NUS Graduate School for Integrative Science and Engineering, National University of Singapore, Singapore 117456

[3]School of Chemical Sciences, Indian Association for the Cultivation of Science (IACS), Jadavpur, Kolkata-700032, India

[4]Department of Physics, Bernal Institute, University of Limerick, Limerick V94 T9PX, Ireland

[5]Fysikum, Stockholm University, 10691 Stockholm, Sweden

[6]Center for Nanoscale Science and Technology, National Institute of Standards and Technology, Gaithersburg, MD 20899-1070, USA

[7]Department of Chemistry, National University of Singapore, Singapore 117543

[8]Centre for Advanced 2D Materials, National University of Singapore, Singapore 117546

[9]Department of Physics, National University of Singapore, Singapore 117542

[10]Department of Electrical and Computer Engineering, Texas A&M University, College Station, TX. 77843. USA

[11]Department of Electrical and Computer Engineering, National University of Singapore, Singapore 117583

[12]Materials Science and Engineering Department, National University of Singapore, Singapore 117575

*Corresponding authors

Section-S1: Chemical characterisation

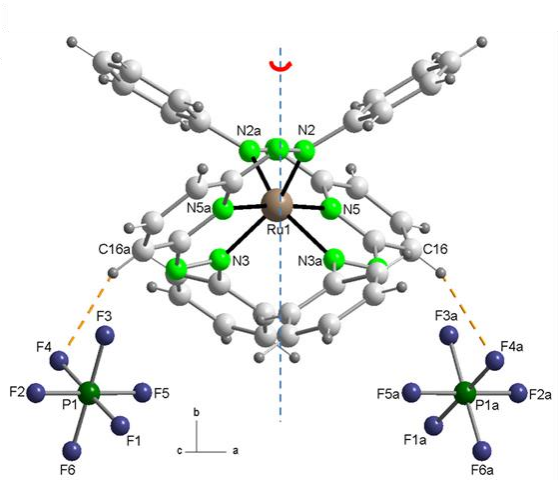

Supplementary Fig. S1 – Molecular view of $[RuL_2](PF_6)_2$: The asymmetric unit of the molecule $[RuL_2]$ $(PF_6)_2$ contains half of a Ru atom, a molecule of ligand (L) and an anion PF_6^-. The molecule is generated by rotation around a two-fold rotation axis. Symmetry transformation used to generate equivalent atoms: a =*-x+1, y, -z+3/2*.

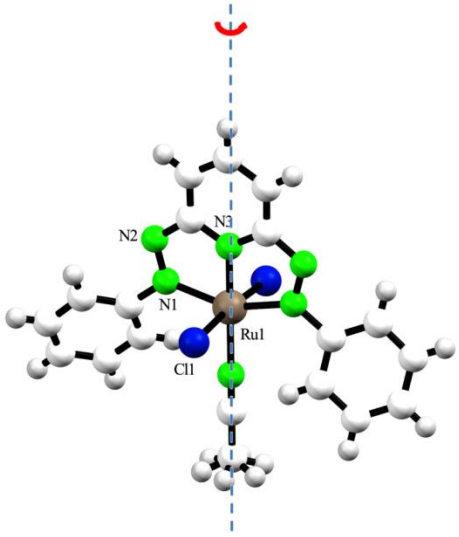

Supplementary Fig. S2 – The asymmetric unit of the molecule [$RuLCl_2(CH_3CN)$] (CCDC deposition code 1913319) contains half of a Ru atom, half of a molecule of ligand (L), a Cl atom and half of a CH_3CN moiety coordinated to the metal centre. A 2-fold rotation axis with direction [0, 1, 0] at 0, y, 1/4 , generates the entire molecule. Symmetry transformations used to generate equivalent atoms:-x,y,1/2-z.

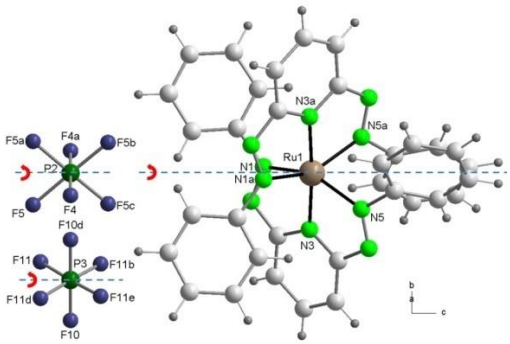

Supplementary Fig. S3 – Molecular view of $[RuL^{(\cdot-)}L]PF_6$ (CCDC deposition code 1840074):The asymmetric unit of the molecule $[RuL^{(\cdot-)}L]PF_6$ contains half a Ru atom, a molecule of ligand (L) and two anionic groups PF_2 with occupancy factors of 0.25 (P), 0.5 (F4/F10) and 1 (F5/F11). A rotation around a two-fold rotation in a direction parallel to the "c" axis, generates the entire cation $[Ru(L_2)]^+$ and two half anions PF_6^-. Symmetry transformations used to generate equivalent atoms: a=*-x+5/4, -y+1/4, z*; b = *x, -y+1/4, -z+1/4*; c =*-x+5/4, y, -z+1/4*; d = *-x+1/4, -y+1/4, z*; e = *-x+1/4, y, -z+1/4*.

Note: The H…F interaction observed in the x-ray structure is not crucial to CD. We confirm this from the following observations:

1. We observed CD with BPh_4 counterion that has no F and hence no H…F bond.
2. Moreover, the activation energy for complexes with BF_4, PF_6 and BPh_4 counterions show a linear relationship with the counterion radii strongly suggesting that the size is important and not the H…F interaction.

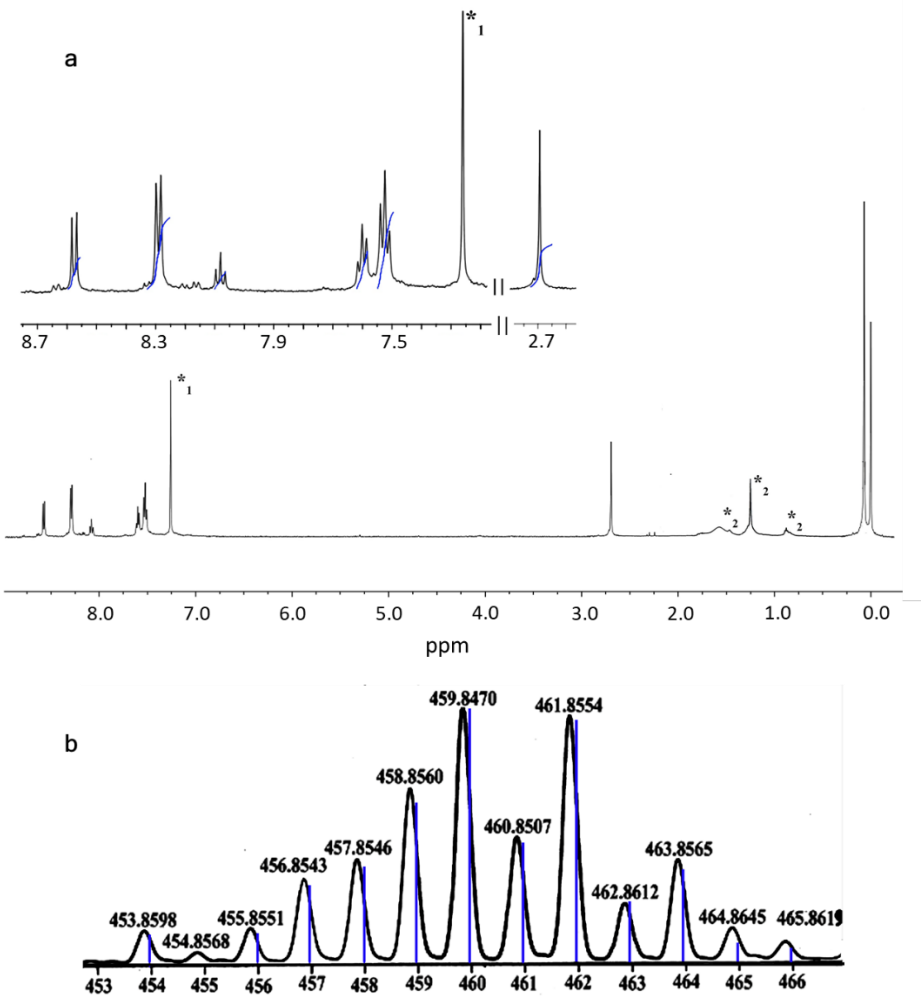

Supplementary Fig. S4 – (a) ^{1}H NMR spectrum of complex [RuLCl$_2$(CH$_3$CN)] in CDCl$_3$ solvent in 400 MHz (*$_1$, solvent residual peak; *$_2$, impurities from solvents) (inset: aromatic proton resonances).

(b) Segmented ESI-MS spectrum of complex [RuLCl$_2$(CH$_3$CN)]; Masses observed from the fragment [C$_{17}$H$_{14}$Cl$_2$N$_5$Ru]$^+$ (z=1), *i.e.*, {[RuLCl$_2$(CH$_3$CN)] - (CH$_3$CN) + H}$^+$. The simulated mass spectrum is in blue.

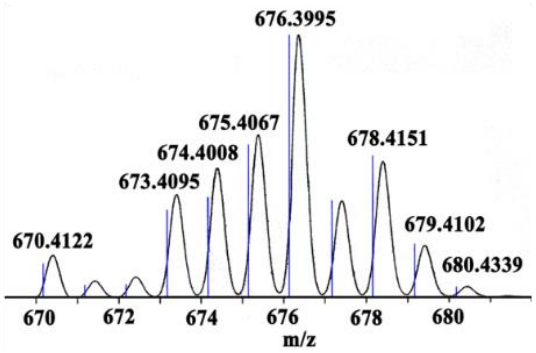

Supplementary Fig. S5 – Segmented ESI-MS spectrum of$[RuL^{(\cdot-)}L]PF_6$; masses observed from fragment $[C_{34}H_{26}N_{10}Ru]^+$ (z=1) i.e.($[RuL^{(\cdot-)}L]PF_6 - PF_6)^+$ (simulated mass spectrum is in blue). This complex is NMR inactive.

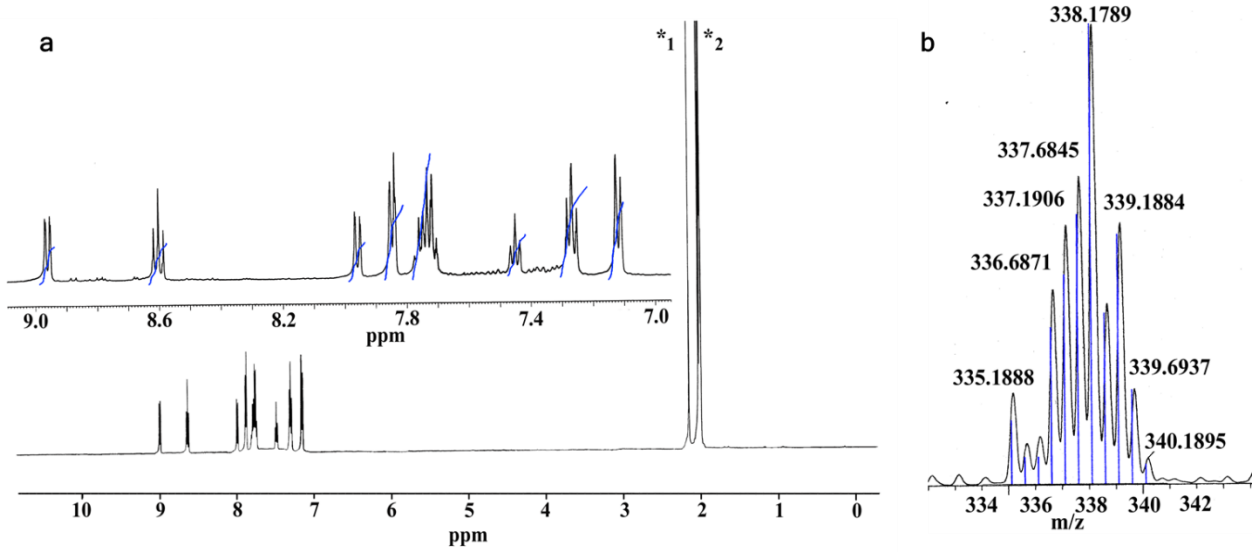

Supplementary Fig. S6 –(a) ^1H NMR spectrum of $[RuL_2](PF_6)_2$ in CD_3CN solvent in 500 MHz ($*_1$, H_2O; $*_2$, solvent residual peak) (inset: aromatic proton resonances).

(b) Segmented ESI-MS spectrum of $[RuL_2](PF_6)_2$; masses observed from fragment $[C_{34}H_{26}N_{10}Ru]^{2+}$ (z=2), *i.e.*, $\{[RuL_2](PF_6)_2 - 2(PF_6)\}^{2+}$. The simulated mass spectrum is in blue.

Section-S2: Ligand centred redox events

Supplementary Table S1: Comparison with redox levels (V) of other molecules used as resistive memory devices[1,2,3,4]

Redox level	Ru-terpyridine[a]	Nitronyl nitoxide[a]	Co(II) polymer[a]	Hybrid polymer[b]	This report[a] (main text Fig. 1a)
Reduction-4					-1.69
Reduction-3			-2.0		-1.19
Reduction-2			-1.75		-0.66
Reduction-1	-1.8	-1.34	-1.45		-0.06
Oxidation-1	0.6	0.22		0.7	
Oxidation-2	0.8			1.2	

[a]All potentials are referenced to Ag/AgCl (saturated KCl)

[b] Pt used as Reference electrode.

Our molecular complex is characterised by four closely spaced, low-lying electron acceptor orbitals that are much lower in energy compared to other reports in the literature (shown in Supplementary Table S1 above), which could be a contributing factor for our observed low voltage and low energy switching.

The CD (or symmetry breaking) observed in our molecule is unique and there is no previous report, to our knowledge where a similar mechanism is observed. As indicated in the main text, we attempted this phenomenon with other Ru complexes of 2,2'-bipyridine, 2,2':6',2"-terpyridine and 2-(phynylimino)pyridine, none of which show CD. In Supplementary Table-S2 we compare the redox levels of these molecular systems to ours.

Supplementary Table S2: Comparison with redox levels (V) of other molecules where CD is not observed.

	Our complex	$[Ru(Tpy)_2]^{2+}$ (reference[5])	$[Ru(bpy)_3]^{2+}$ (reference[6])	$[Ru(PIP)_3]^{2+}$ (reference[6])
Oxidation 1		1.32	1.36	1.47
reduction 1	-0.06	-1.22	-1.26	-0.89
reduction 2	-0.66	-1.46	-1.45	-1.12
reduction 3	-1.19		-1.69	-1.45
reduction 4	-1.69			

All potentials are referenced to Ag/AgCl (saturated KCl)

Tpy= 2,2';6',2''-terpyridine

bpy= 2,2'-bipyridine

PIP= 2-(phenylimino)pyridine

Notably, CD requires the accessibility of multiple redox energy levels necessitating presence of low lying and closely spaced LUMO+n orbitals. As established in Supplementary Table-S2, the redox levels in our complex are much lower compared to the other ligand-based complexes and hence are accessible in a reasonable voltage range. That makes CD favourable in our film. In fact, even redox events are difficult to observe in films of $Ru(bpy)_3$, $Ru(Tpy)_2$ and $Ru(PIP)_3$ (probed by other groups as well[7]) let alone a CD mechanism.

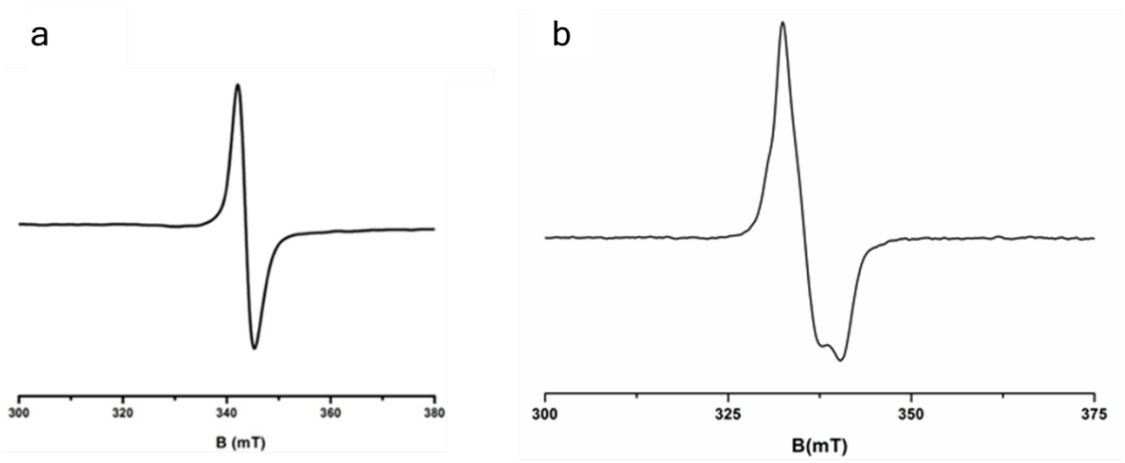

Supplementary Fig. S7 – (a) X-band electron paramagnetic resonance (EPR) spectrum (g=1.965) of $[RuL^{(\bullet-)}L]PF_6$ in dichloromethane solution at 298K. (b) X-band electron paramagnetic resonance (EPR) spectrum (g1=1.975, g2=1.946, g3=1.918; gav=1.947) of electrogenerated one electron reduced species, $[RuL^{(\bullet-)}L]PF_6$ (bulk electrolysis at -0.35 V *vs.* Ag/AgCl reference electrode using supporting electrolyte $[Bu_4N]PF_6$) in dichloromethane-toluene glass at liquid nitrogen temperature (77K).

The broadening of the EPR peak (g=1.965) at 298K can be ascribed to d-p (metal-ligand) mixing indicating the contribution of the metal in the LUMO[8,9,10,11]. However, the absence of anisotropy (very low g-anisotropy, Δg=0.057 even at 77K) in this spectrum eliminates the possibility of a major metal contribution. Hence, we conclude the redox event to be primarily ligand centred with a minor metal contribution. This is also supported by our spectroscopic observations. The Ru^{2+}/Ru^{3+} transition would result in low energy absorption peaks beyond 800 nm[12,13,14,15,16] which we never observed in our voltage scan range.

Section-S3: Film characterisation

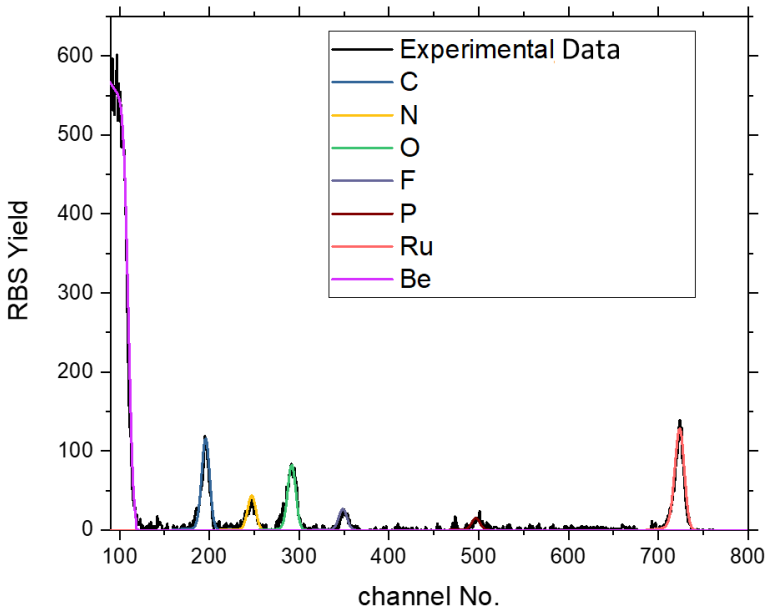

Supplementary Fig. S8 – Rutherford Back Scattering spectrum of the $[Ru(L)_2](PF_6)_2$ film giving a molecular density of 8.2×10^{12} molecules/cm^2.

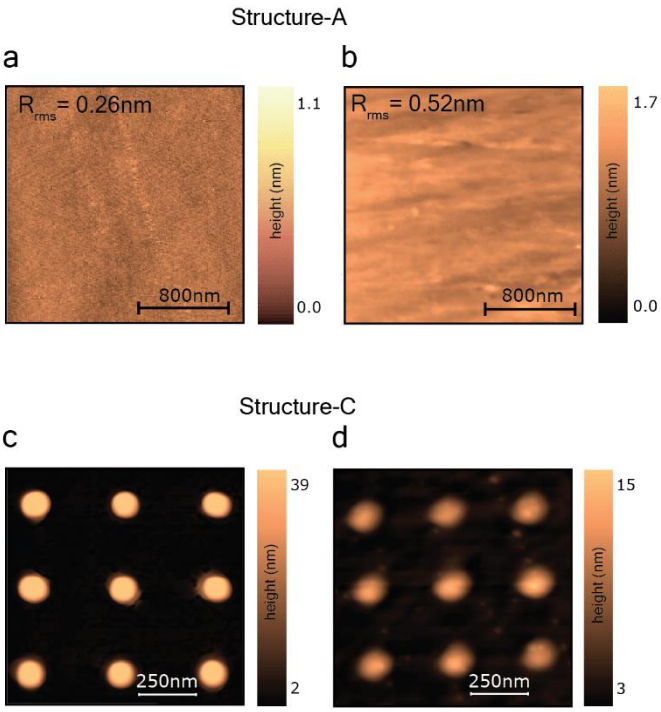

Supplementary Fig. S9 – (a) Topography of the indium tin oxide (ITO) film measured by atomic force microscopy (AFM). The film is epitaxially grown on Yttria stabilized Zirconia (YSZ) substrate.

(b) AFM-topography of the spin coated film of $[Ru^{II}L_2](PF_6)_2$ on ITO.

(c) AFM-topography of lithographically patterned gold nano-discs on ITO (used as bottom electrodes for the devices in Fig.2a (nano disc diameter = 100 nm).

(d) AFM-topography of spin-coated film of $[Ru^{II}L_2](PF_6)_2$ on the nano-discs.

Note: The film thicknesses in the micro and nano devices are the same (35±4 nm) (in nano-devices the film thickness measurement process is illustrated in Supplementary Fig. S10). As established elsewhere[17], for a c-AFM measurement with a CSC17/Ti-Pt tip (resonant frequency ~12 kHz, force constant ~0.15 N/m) on a film of a Ru-complex of azo-aromatic ligand, the typical penetration of the tip into the film is <4nm which is insufficient to produce any significant thickness change of our film. The difference in voltage arises from the enhanced electric field at the interface of the nano-structures and the film. A similar technique has been utilised in other reports[17,18].

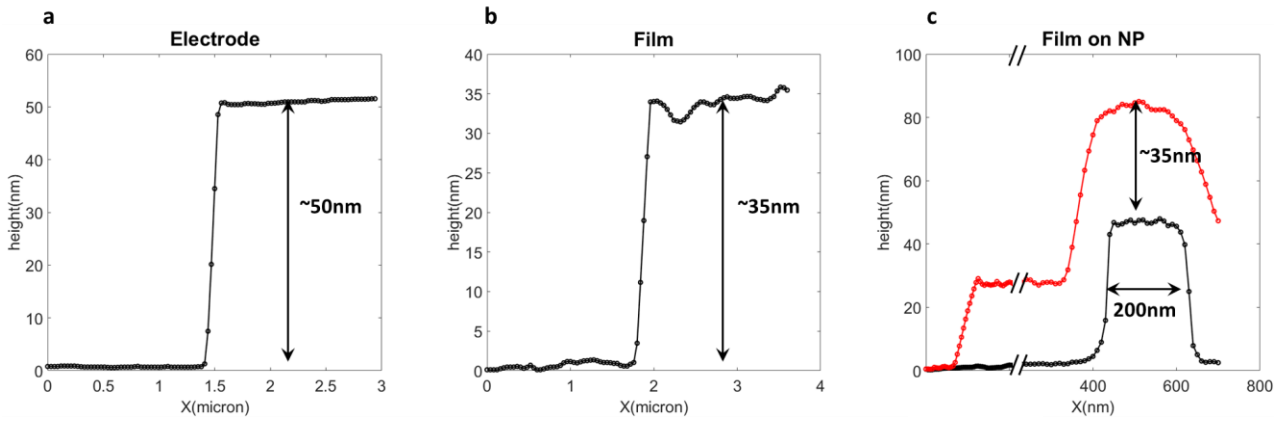

Supplementary Fig. S10 – (a) Electrode thickness and (b,c) film thickness measurement by AFM in (b) structure-A and (c) structure-B.

Section-S4: Additional device characterisation

Thickness dependent *J(V)s* from structure – A and B:

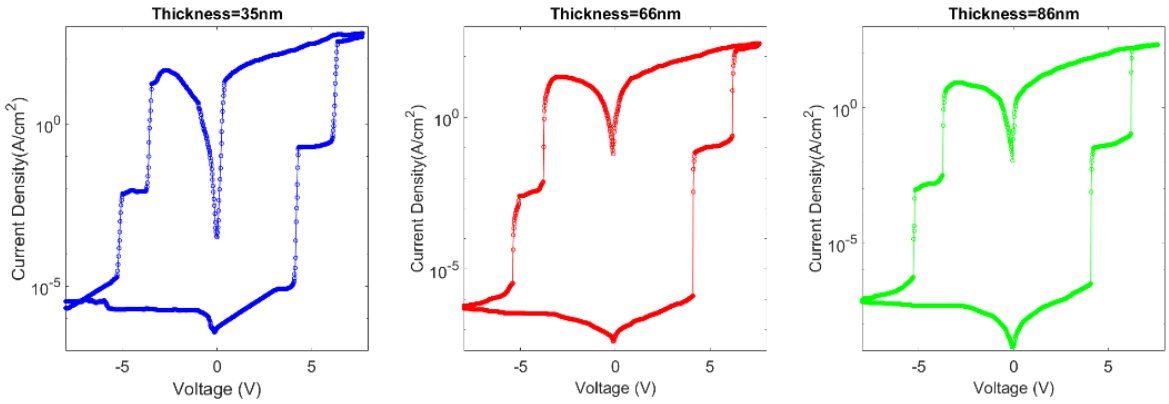

Supplementary Fig. S11 – Thickness dependent *J(V)* of structure-A

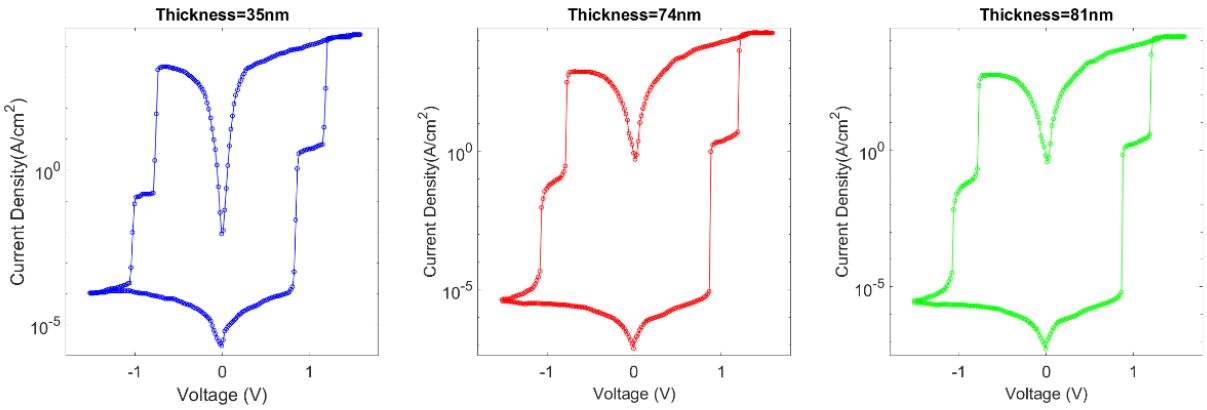

Supplementary Fig. S12 – Thickness dependent *J(V)* of structure-B

Note: Following redox mechanism, the switching voltage should depend on electrode level alignment with the film energy levels. Hence, the switching voltage values are overall insensitive to the film thickness – consistent with redox. Devices of all thicknesses are fairly stable and robust. We made devices in 4 different batches and they are reproducible.

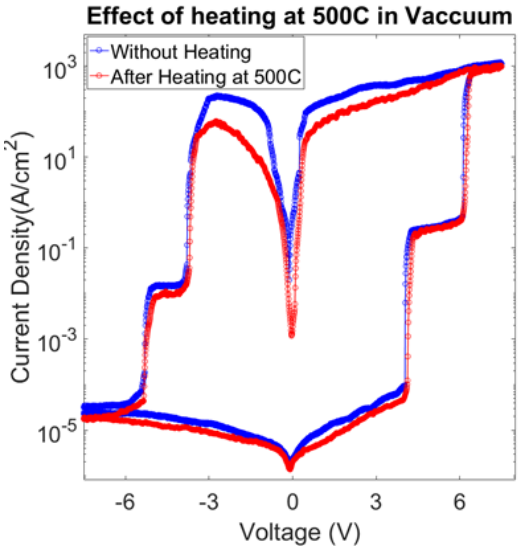

Supplementary Fig. S13– *J(V)*s of structure-A before and after heating (at 500 °C in vacuum) - No degradation observed.

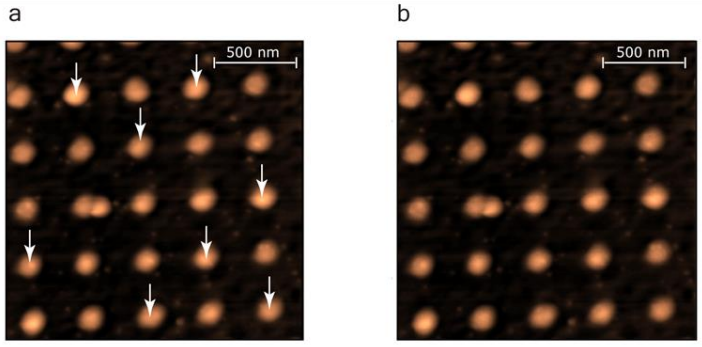

Supplementary Fig. S14 – (a) Topography of molecular film before c-AFM-measurements. Arrows indicate the points where measurements were performed.
(b) Topography of molecular film after c-AFM measurement confirming that our measurements have not caused damage to the film[17].

Note: The film topography before and after the *I(V)* measurements, presented in Supplementary Fig. S14a,b shows that we do not observe any blurring or artefacts due to tip damage. In fact, we measured the *I(V)* several times on the same locations and between measurements we retracted and then approached the tip. This eliminates tip induced artefacts in our *I(V)* measurements[17].

Calculation of switching energy:

Switching energy for the nano-device is calculated using $E_{sw} = V_{sw} \times I_{post-sw} \times t_{sw}$ (V_{sw}= switching voltage, $I_{post-sw}$ = current after switching, t_{sw}= switching time)

For switching from the 3 1 state- to the 1 1 state:

$$E_{sw1} = 0.149V \times (40.39 \times 10^{-9})A \times (30 \times 10^{-9})s \sim 200\text{aJ}$$ and

for switching from the 1 1 state to the 0 0 state

$$E_{sw2} = 0.211V \times (5.36 \times 10^{-6})A \times (30 \times 10^{-9})s \sim 30\text{fJ}.$$

Switching time is assumed as 30ns. In the current response to a pulse of rise time 30 ns we observe a current overshoot (see Extended Data Fig. 4a) suggesting that the switching speed of our device is less than the rise time, *i.e.* <30ns. Structure-C should be even faster due to its lower resistivity value. Hence the values used to estimate switching energy of device-C are highly conservative and calculated energy values are overestimated.

Section-S5: Switching Uniformity

Our switching is uniform, and possibility of a filamentary switching can be ruled out based on the following evidences:

(I) Our device current scales with area. This is just opposite to filamentary switching which must be area-independent. Note, the current densities in device-A, B and C cannot be compared, because, the nano-structures in structure-B, C cause an electric field enhancement in the device, as elaborated in section-S7. The field inside these structures being very different, the current densities must be different too. Hence, to conclude on scalability, different sizes of same structure (i.e. all device-A or all device-B) should be compared.

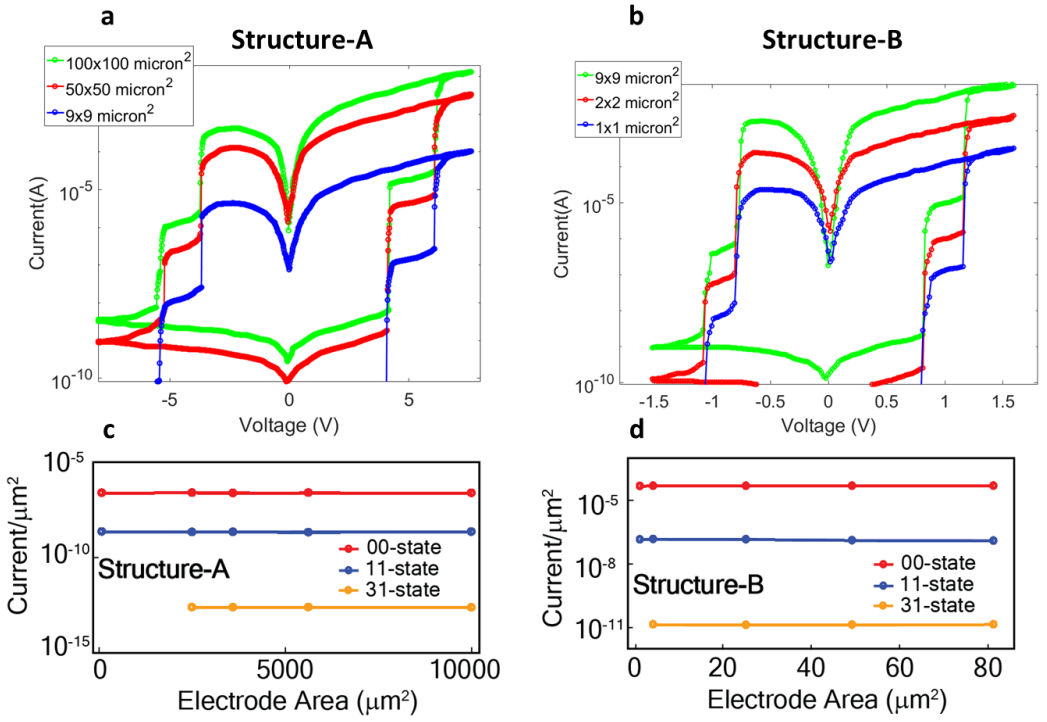

Supplementary Fig. S15 – (a,b) The electrode size dependent *I(V)* for (a) structure-A and (b) structure-B showing areal current scaling.

Note: current values below 10^{-10}A is not shown as those values approach the sensitivity limit of our set up and are not reliable. Also, the areas chosen to show areal scalability of current for structure-A and B are different. This is because the current density in these two structures are different and are caused by the difference in electric field (due to field enhancement) inside the

structure (discussed in section-S7). Because structure- B has a much higher current density than structure-A, to keep current values within measurable limits, lower areas have been chosen for structure-B.

(c,d) The current densities plotted for different electrode sizes of (c) structure-A and (d) structure-B. For the lower dimensions we have not reported the current value of the (31) state because the values become too low compared to the instrument range.

The areal current scaling observed here strongly suggests the switching uniformity.

(II) The c-AFM imaging of our film surface shows that the entire film switches uniformly. In Supplementary Fig. S16 we show the structure used for this measurement, in which the bottom electrode was either a flat ITO or an ITO with lithographically designed nanostructures. Consistent with characterizations performed on the structure-C, this geometry also allows the film to switch, just like structures-A and B and this structure enables us to spatially map the current characteristics as a function of applied bias on the tip. This is possibly the cleanest method to probe switching uniformity where there is no top electrode to be removed.

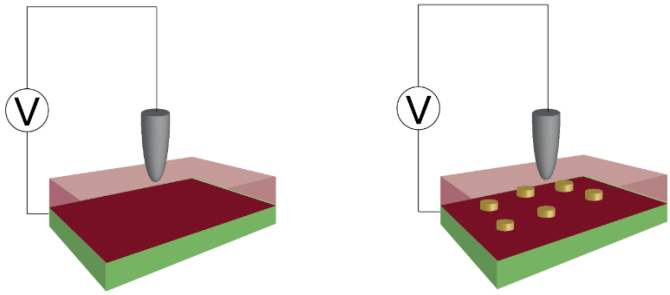

Supplementary Fig. S16 – The c-AFM measurements where performed in contact mode (*i.e.* the tip in contact with the film surface)

The current scans obtained from these two structures presented in Supplementary Fig. S16 (*i.e.* flat bottom ITO or ITO with nano-structures) are shown in Supplementary Fig. S17. It is evident that in both these structures, 100% of the film area (scanned over 25×25 μm^2) undergoes switching. Notably, the current variation in the c-AFM scan of each state is <0.5% of the ratio between any two of the conductance states.

However, for the devices with nano-structured bottom electrodes, the switching started from the edges of the nano-structures, where the field enhancement is maximum. At higher applied voltage values the switching spread across the entire film. A detailed description of this spatial switching evolution requires spectroscopic examination, which can be probed with tip enhanced Raman spectroscopy (TERS). These issues are beyond the scope of this paper and will be discussed elsewhere.

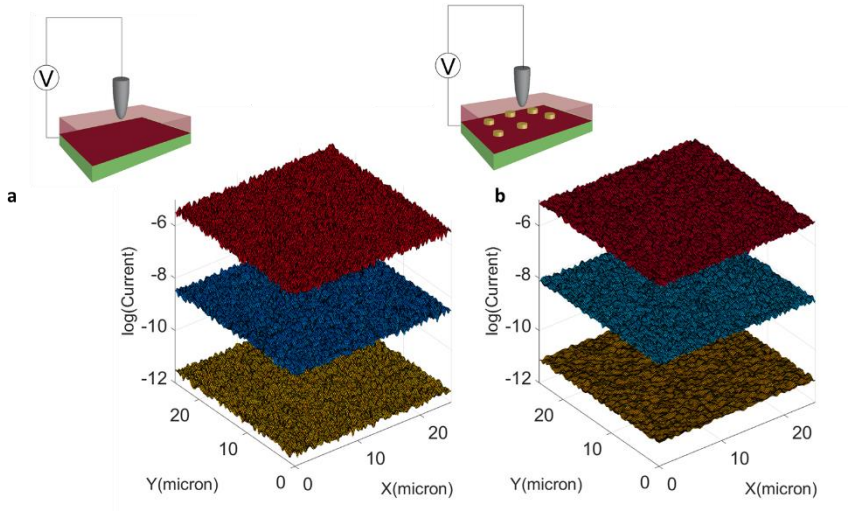

Supplementary Fig. S17 – The current scan on devices with (a) flat and (b) nano-structured bottom electrodes with a c-AFM tip as the top-electrode in contact with the film during the scan.

Section-S6: Elimination of the possibility of an interfacial mechanism

An existing report[19] suggests that oxygen plasma treatment of ITO changes the stoichiometry at the ITO surface, driving a resistive switching *via* oxygen filament formation. Since we used an oxygen plasma to clean the surface, we tested an oxygen plasma treated ITO sample with just an Au contact. We saw no resistive switching (see Supplementary Fig. S18) in the absence of a molecular film, consistent with previous reports on metal-ITO contacts[20]. This control measurement excludes the possibility of contribution of the ITO interface to the switching.

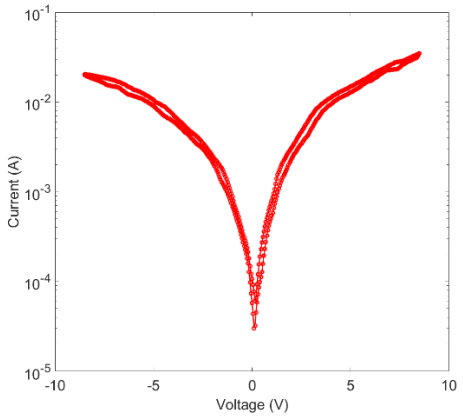

Supplementary Fig. S18 – The I-V characteristics of the Au/ITO junction with no molecular film – no resisting switching was observed.

Also, if a switching mechanism is interface driven, then the observation should be specific to a particular interface. Extended Data Fig. 6 shows the memristive *J(V)*s produced by devices with different electrode combinations, *viz.* Pt/film/Pt, Au/film/ Au and Au/film/Pt (read as top electrode material/ film/ bottom electrode material), all producing qualitatively similar *J(V)*s.

So, in total, we present ternary memristive *J(V)*s for 5 different electrode combinations (written as top electrode material/ film/ bottom electrode material), *viz.*

1. Au/film/ITO
2. ITO/film/IO
3. Pt/film/Pt
4. Au/film/Pt
5. Au/film/Au

demonstrating that the switching properties of the molecular film are independent of the electrode combination.

In summary, an interfacial mechanism can also be ruled out based on our following observations:

a. An interfacial mechanism cannot change the film polarizability. In Supplementary Fig. S25, we have shown that the permittivity-voltage ε (V) characteristics can be fitted with Johnson's model[21] and not with Clausius-Mosotti relation[22] proving that the capacitance arises from highly interacting dipoles, which is a film effect and not an interfacial effect.
b. An interfacial mechanism cannot explain change in Raman and UV-Vis spectral traces that occur concurrently with the current and capacitance switching.
c. An interfacial or any other related mechanism cannot explain the field cooling and zero field cooling (FC and ZFC) *J(V,T)* profiles shown in Fig. 5c,d.
d. Finally, the temperature dependence of the memristive states shows a linear correlation with the size of the counterions used in the molecular complexes (see Fig. 6). It is impossible to explain molecular size dependence with an interfacial model – it can only make sense if this is related to a bulk film effect.

Section-S7: Role of Nanostructures

In a nano device the current density is much more than in a micro-device because the field values inside these devices are very different. The nano-structure causes an electric field enhancement (the value can be higher than 25× depending on the geometry). Owing to the presence of confined and enhanced electric field, nano structures can significantly reduce charge injection barrier between a metal and a semiconducting film as established in several previous reports[17,23,24,25,26]. In between a spin coated film and an electrode, inevitably, there will be a charge injection barrier which is a problem in every organic device. The interfacial electric field enhancement at the nano-structure overcomes the barrier and hence the current value in each plateau goes higher and the switching voltage values reduce. Supplementary Fig. S19 compares the field values in 4 different structures used in this discussion.

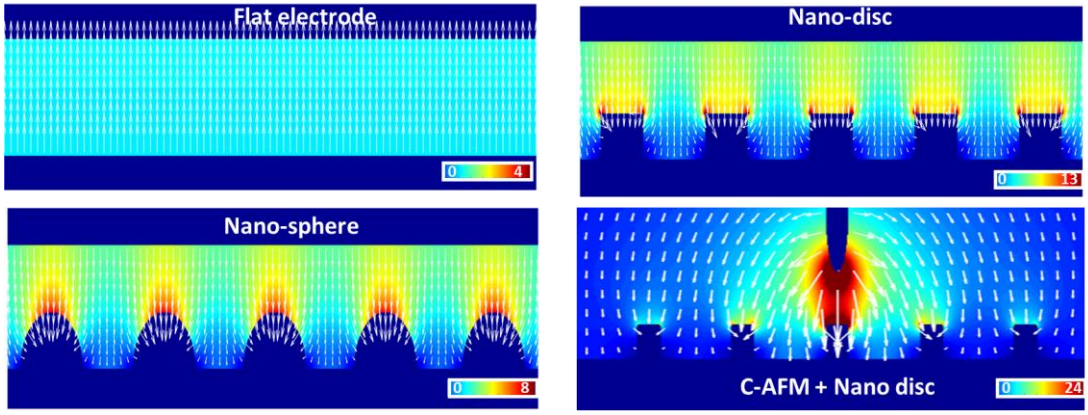

Supplementary Fig. S19 – Electric field enhancement on a nano structure. In structure-C we observe an enhancement of >24 times and in structure-B, the observed enhancement is around 13. Note, in real c-AFM structure, the tip ideally should contain a few atoms and hence the edge is sharper and the enhancement value can be even higher than 25×.

To further substantiate that the current enhancement is caused by the field enhancement on the nano-structures, we provide additional evidences:

1. We took two devices of 3×3 micron^2 of structure-A and B. If it was an effect of lateral scaling, the current and switching voltage values should be identical. The measured *J(V)* for both the devices are now presented below.

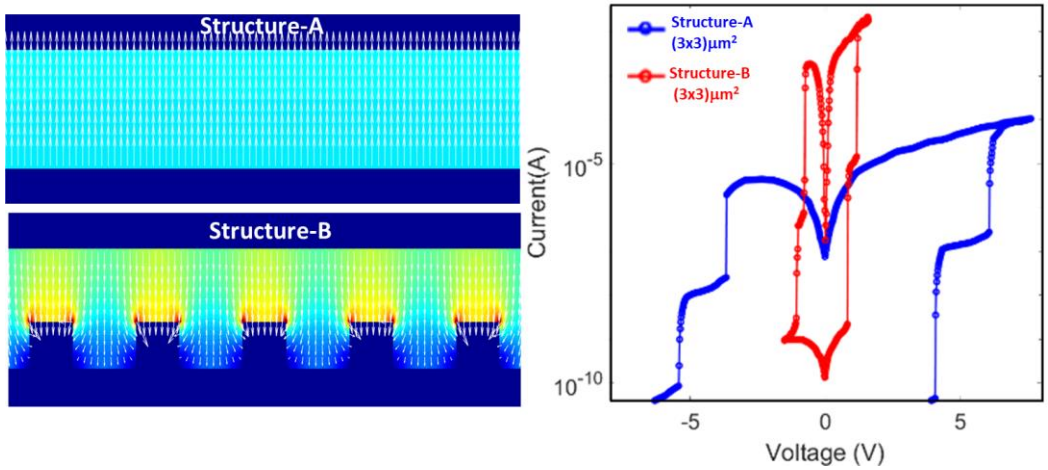

Supplementary Fig. S20 – *J(V)* of two 3×3 μm^2 devices of structure-A and B. Note that, we did not show the data below 10^{-10} A because current below that is noisy and may lack reliability.

It is very clear that, both current enhancement and voltage reduction is caused by the field enhancement at the nano-structures.

2. We have taken two devices (structure-B) of identical size – one with nano-discs with edges and the other with nano spheres (of identical areal density). Clearly, the only difference here is the electric field enhancement. As shown in our calculation, in nano-disc, due to presence of edges, the field enhancement is about 13 times, compared to a factor of 8 for nano-spheres. This accounts for a larger current enhancement and lower switching voltage values in the nano-disc structure. This proves that it is the field enhancement that reduces the charge injection barrier between the electrode and the film and that is what determines the device voltage and current range.

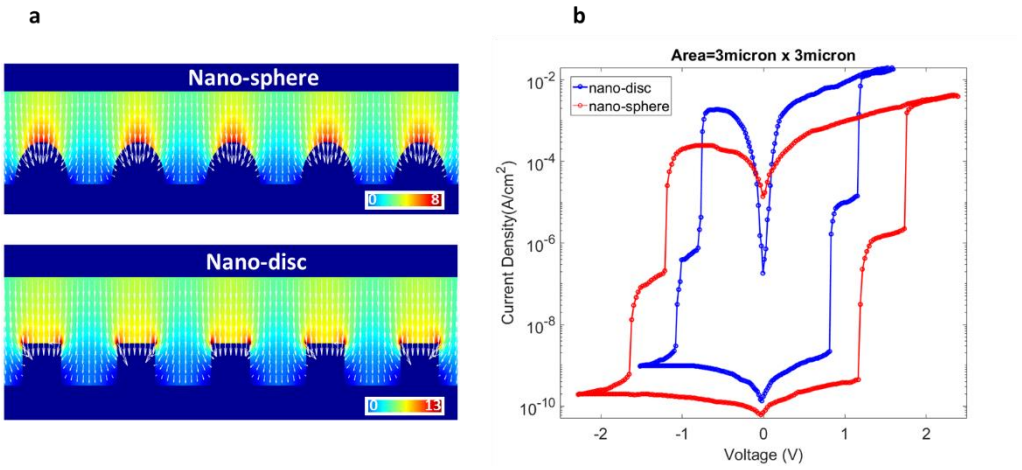

Supplementary Fig. S21 – (a) Field enhancement on nano-particles and nano-discs, (b) *J(V)* of two devices – one with nano-particles and the other with nano-discs both with 9μm^2 device area.

Section-S8: Device statistics

295 samples of structure-A were prepared in 20 different batches. For structure-C, multiple measurements were performed on 18 different areas in 3 different samples (on > 54 different nano-structures) which were lithographically patterned in different batches. Our results establish a device to device reproducibility and consistency significantly better than the existing literature.

Supplementary Table S3: Device statistics of micro and nano ternary-devices: summary of results

Structure-A

Size (μmxμm)	# Devices	Film Thickness (nm)	Switch-on Voltage (V)	Switch-off voltage (V)	Current density (A/cm^2) V_{read}=2V				Ratio
					On	Int1	Int2	Off	
100 x 100	117	58±4	Sw 1: 4.3±0.2 Sw 2: 6.2±0.2	Sw 1: -3.5±0.2 Sw 2: -5.1±0.3	(6.6±0.5) x 10^{1}	(7.8±1.2) x 10^{-2}	(8.8±0.7) x 10^{-3}	(2.9±0.5) x 10^{-6}	On/ Int1 ~10^{3} Int1/ Int2 ~10 Int2/ Off ~10^{3}
80 x 80	39								
60 x 60	34								
40 x 40	29								
20 x 20	31								
10 x 10	22								
1 x 1	23								

Structure-C

Number of measured points	Device area	Thickness (nm)	Switch-on voltage (mV)	Switch-off voltage (mV)	Current (A/cm^2) V_{read}=75mV				Ratio
					On	Int-1	Int-2	Off	
54	~60nm^2	42±4	151±6 215±7	-135±6 -186±5	(2.7±1.2) x10^{6}	(3.1±0.7) x10^{3}	(6.6±0.8) x10^{2}	(7.1±1.2) x10^{-1}	On/Int1 ~10^{3} Int1/Int2 ~5 Int2/Off ~10^{3}

***** Int-1and Int-2 are the positive and negative intermediate states respectively.

Section-S9: Comparison with other devices

As tabulated below, there has been several reports on write-once, read-many (WORM) devices. The observed *I(V)* responses are irreversible and hence the states are not rewritable. Unlike memristors, these structures have only a limited set of applications.

Supplementary Table S4: Comparison with other ternary devices in literature

Info source	Material	Reproducibility	Endurance	Stability (s)	On/off	states	On- and Int-state resistance	Switching time	Switching voltage
Mater. Horiz., 2014, 1, 446	Oxacalix[4]arene	2 devices	Not rewritable	$4x10^4$	$1:10^{4.2}:10^{8.7}$	3	16 GΩ 1600 TΩ	No info	-1.8V -2.7V
J. Am. Chem. Soc. 2016, 138, 6368–6371	Phosphole Oxide-Containing Organogold(III) Complex	No info	Not rewritable	7500	$1:10^3:10^7$	3	125 GΩ 6.3 TΩ	No info	1.5V 2.5V
J. Am. Chem. Soc. 2013, 135, 14086–14089	Heteroacene	No info	Not rewritable	10^4	$1:10^{4.3}:10^{6.3}$	3	16 GΩ 1 TΩ	No info	-2.5V -3.25V
J. Am. Chem. Soc. 2017, 139, 7256–7263	Peripherally functionalized subphthalocyanines	No info	Not rewritable	10^4	$1:10^6:10^8$	3	~60 GΩ ~60 TΩ	No info	2V 2.5V
J. Am. Chem. Soc. 2012, 134, 20053–20059	Meta-conjugated donor-bridge acceptor (DBA) molecule	No info	Not rewritable	$5x10^4$	$1:10^3:10^6$	3	50 TΩ 10^4 TΩ	No info	1.2V 1.8V
J. Phys. Chem. C 2012, 116, 25546–25551	Copolymers with Pendent Carbazole and Nitro-Azobenzene	No info	Not rewritable	10^4	$1:10^{2.5}:10^{4.5}$	3	8 GΩ 1TΩ	No info	-1.75V -5.5V
J. Am. Chem. Soc. 2010, 132, 5542–5543	Azo-based molecules	No-info	Not rewritable	No info	$1:10^2:10^6$	3	~16 GΩ ~400 TΩ	No info	-1.5V -2.2V
Mater. Horiz., 2014, 1, 446	Oxacalix[4]arene	2 devices	Not rewritable	$4x10^4$	$1:10^{4.2}:10^{8.7}$	3	16 GΩ 1600 TΩ	No info	-1.8V -2.7V
J. Am. Chem. Soc. 2016, 138, 6368–6371	Phosphole Oxide-Containing Organogold(III) Complex	No info	Not rewritable	7500	$1:10^3:10^7$	3	125 GΩ 6.3 TΩ	No info	1.5V 2.5V
J. Am. Chem. Soc. 2013, 135, 14086–14089	Heteroacene	No info	Not rewritable	10^4	$1:10^{4.3}:10^{6.3}$	3	16 GΩ 1 TΩ	No info	-2.5V -3.25V
J. Am. Chem. Soc. 2017, 139, 7256–7263	Peripherally functionalized subphthalocyanines	No info	Not rewritable	10^4	$1:10^6:10^8$	3	~60 GΩ ~60 TΩ	No info	2V 2.5V
J. Am. Chem. Soc. 2012, 134, 20053–20059	Meta-conjugated donor-bridge acceptor (DBA) molecule	No info	Not rewritable	$5x10^4$	$1:10^3:10^6$	3	50 TΩ 10^4 TΩ	No info	1.2V 1.8V
J. Phys. Chem. C 2012, 116, 25546–25551	Copolymers with Pendent Carbazole and Nitro-Azobenzene	No info	Not rewritable	10^4	$1:10^{2.5}:10^{4.5}$	3	8 GΩ 1TΩ	No info	-1.75V -5.5V
J. Am. Chem. Soc. 2010, 132, 5542–5543	Azo-based molecules	No-info	Not rewritable	No info	$1:10^2:10^6$	3	~16 GΩ ~400 TΩ	No info	-1.5V -2.2V

Info source	Material	Reproducibility	Endurance	Stability (s)	On/off	states	On- and Int-state resistance	Switching time	Switching voltage
J. Phys. Chem. C 2012, 116, 22832–22839	Twisted Anthraquinone (azo-based)	No info	Not rewritable	10^4	$1:10^{3.5}:10^{5.5}$	3	8 GΩ .5 TΩ	No info	-1.5V -2.75V
Angew. Chem. Int. Ed. 2015, 54,10569 –10573	D-A Compound Containing Boron(III)	20 devices	Not rewritable	10^4	$1:10^3:10^6$	3	600 GΩ 3000 TΩ	No info	2V 3.2V
Advanced Materials 27.39 (2015) 5968-5973	OZO-SO, OZA-SO	No info	Not rewritable	10^4	$1:10^{3.4}:10^{6.2}$	3	1.5 GΩ 1 TΩ	No info	-1V -3.7V
Adv. Mater. 2012, 24, 6210–6215	conjugated small molecules	No info	Not rewritable	$4x10^4$	$1:10^2:10^4$	3	50 GΩ 25 TΩ	No info	-1.5V -2.7V
Nanoscale, 2017, 9, 10610	Conjugated polymer + graphene oxide quantum dots	No info	Rewritable 600 cycles	10^4	1:60:3000	3	80 GΩ 8 TΩ	No info	-1.2V -2V
J. Mater. Chem. C, 2017, 5, 8593	Polymethacrylate containing pendent azobenzene–naphthalene	No info	No info	10^4	$1:10^2:10^3$	3	15 GΩ 0.5 TΩ	No info	3V 3.7V
Scientific Reports 7.1 (2017): 3938.	Graphene oxide in Polystyrene	No info	10^4	10^5	$1:10:10^3$	3	.23GΩ 35GΩ	>sec	1V 1.7V
Our Device (scaled for 20nmx20nm)	**Ru-complex of a azo-aromatic ligand**	**300 devices**	**10^{10}**	**10^6**	**$1: 10^4:10^7$**	**3**	**20kΩ 2.5MΩ**	**<30ns**	**151±6 mV 215±7 mV**
Our Device Estimated area= 60nm^2 (measured values)	**Ru-complex of a azo-aromatic ligand**	**300 devices**	**10^{10}**	**10^6**	**$1: 10^4:10^7$**	**3**	**160kΩ 20MΩ**	**<30ns**	**151±6 mV 215±7 mV**

Endurance: The number of write-read-erase-read cycles

Stability: Temporal persistence of conductance states with constant application of reading voltage at 350K

On-state and intermediate-state resistance: Numbers are normalised for a 20nm×20nm device area (typical industrial size) for comparison purposes.

From Supplementary Table S4 we conclude the following:

- According to the mathematical framework of memristors, developed by Leon Chua, a device needs to form pinched hysteresis loop in *I(V)* plane to be termed as a memristor[27]. WORM devices are not memristors as they do not satisfy that criterion.
- The two primary applications of a memristor are as RRAM and for logic – both demand re-writability. WORM devices are not rewritable and hence are unsuited for either of these applications. The only possible application area of such devices could be as read only memories (ROM).
- However, the problem is, when scaled to even a μm^2 area, the intermediates state current in these devices (21 such reports are presented in Supplementary Table-S4) go <1nA which is too low and is not useful for any circuit (according to ITRS standard).
- If we further scale the currents to $2500nm^2$ (a fairly large area compared to real devices) then even the on-state current goes < 1nA.

  In summary, these current values are too small to be sensed and hence these devices are not scalable.
- The switching voltages of these devices are ~3V, too high and the variation values are also exorbitantly high for any practical purpose.

Although a molecular mechanism implies a uniform areal switching, it has never been observed in these devices. In fact, to our knowledge, no organic device until now has ever shown a 100% areal switching.

We show below c-AFM images, taken from 4 independent measurements on organic memristors/ WORM devices with multiple states from the following papers:

1. J. Mater. Chem., 2012, 22, 16582
2. Nanoscale. 9: 10610-10618, 2017
3. Scientific reports 5 (2015): 10022
4. Scientific reports 6 (2016): 38816

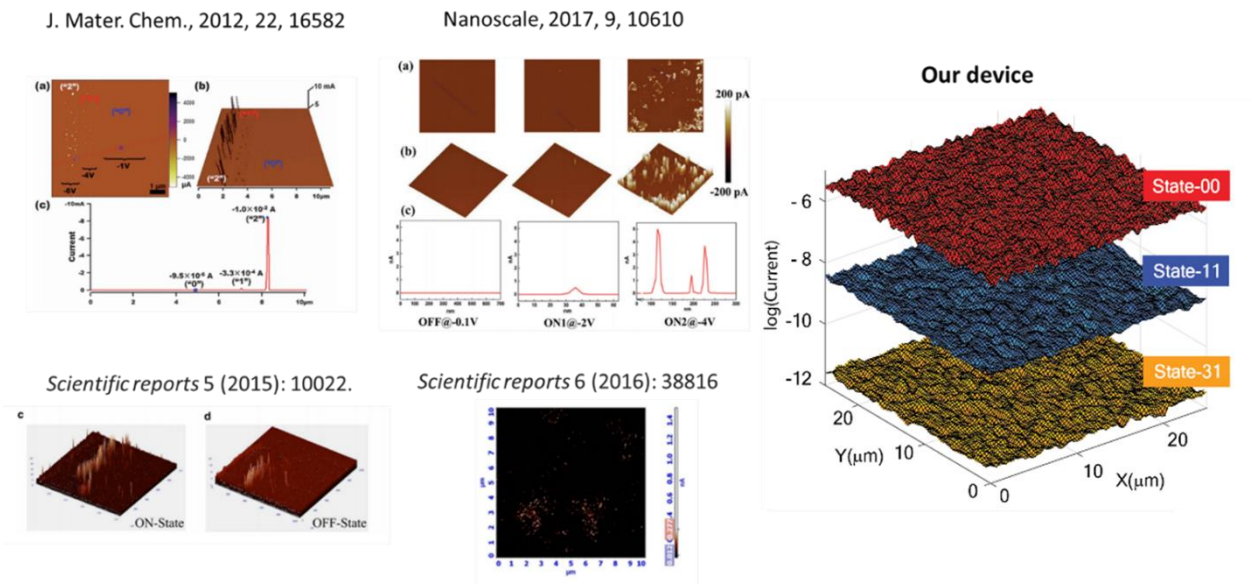

Supplementary Fig. S22 – A comparison between c-AFM images of other organic devices and the present device. We have taken permission from Royal Society of Chemistry[28,29] and Nature Springer[30,31] for the re-use of the figures for comparison.

All the data shown in Supplementary Fig. S22 only show non-uniform spikes akin to noise that usually arise either from filaments or from improper grounding of the bottom electrode. Looking at these measurements, we conclude that while molecular mechanisms are proposed for these devices, they are unreliable and these switching processes most probably arise from interfacial defects or filaments. In contrast, the present c-AFM data shows switching of 100% of the film surface – a demonstration lacking in any of the existing publications and representing a major advancement in itself.

Comment on the memcapacitive device by Bessonov *et.al.*:

We have noted a report[32] by Bessonov *et.al.* on a capacitive memory showing an enhancement in capacitance with a decrease in resistance. Their model showing a memristor and a memcapacitor in parallel would imply device resistance to go up with an increased capacitance. The only way this can possibly be explained is using a combination of memristors and capacitors, as shown by

Wang *et.al.* [33]. They call it a *pseudo*-memcapacitor as it does not arise from a single device property but from a lumped element circuit.

Supplementary Table S5: Comparison with ITRS, 2015 projected values

Parameter	ITRS Projection (adopted from Table ERD4b, ITRS-2015)	Achieved Values (measured in structure-C)
Read Current	>10nA/ 100pA (unipolar/ bipolar)	5µA (On), 40nA(Intermediate) (at .1V)
W/E time	~ns	~30ns
Write Cycles	$>10^{10}$	$> 10^{10}$
Write Voltage	<0.6V	0.15V, .22V
Read Voltage	<0.2V	<.1V
Write energy	<1pJ	200aJ, 30fJ (area 60 nm^2)

Section-S10: Calculation of Energy Levels using Periodic DFT

The MO eigenvalues and eigen surfaces are identical, to within 10 meV and when visualized using an iso value=0.1 au, respectively, in the 4-molecule unit cell based on the X-ray structure and 8 molecule unit cell based on a 2×1×1 supercell of the X-ray structure. Hence the data in Fig. 1 would be simply duplicated as shown in Supplementary Fig. S23 below. For the data in Fig. 5, the ΔE values change by <10 meV and the displacements by <0.02 Angstrom so the plots are perfectly superimposed.

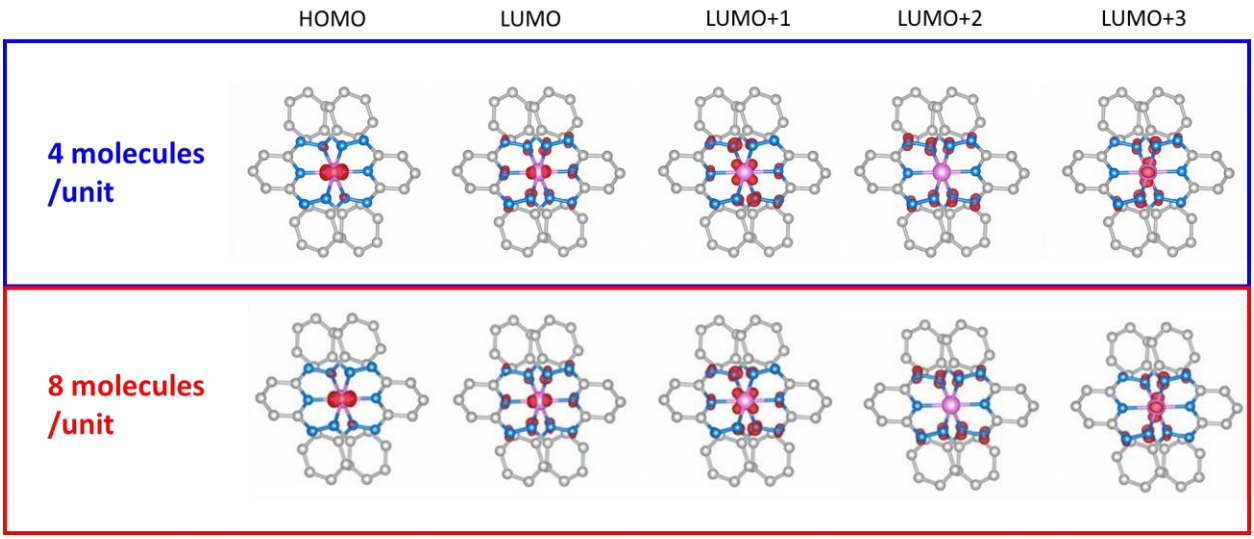

Supplementary Fig. S23 – Molecular orbitals derived for four- and eight-molecule unit cells.

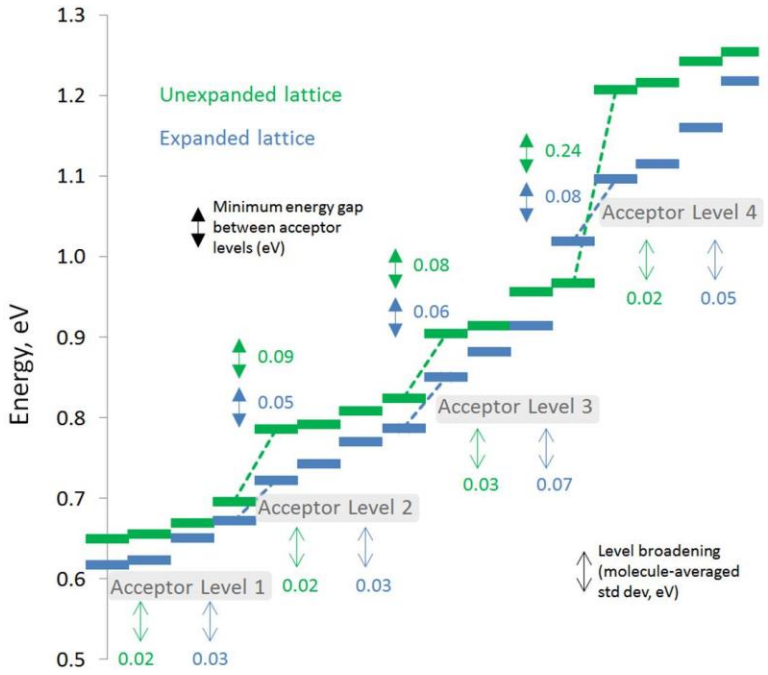

Supplementary Fig. S24 – Shown above are the calculated molecular energy levels in expanded and unexpanded lattice of $[RuL_2](PF_6)_2$. In the expanded lattice (that enables larger counterion displacements), a clear broadening of levels is observed (four molecule unit cell, so four mini-levels at each reduction level) which gives a contraction in energy gap between reduction levels. Not all counter ions follow the exact same displacement vector away from the molecules, which creates a broader distribution. This means that in an expanded system (representing a film) the observation of a switching voltage lower than the CV potentials is not surprising and that is what we observe in structure-C.

Section-S11: Permittivity fitting

The field-dependent dielectric constant of the film was fitted with two alternate functions:

1. **Johnson's equation**: $\varepsilon_r(E) = \frac{\varepsilon_r(0)}{1+\{\lambda(\varepsilon_0\varepsilon_r(0))^2E^2\}^{\frac{1}{3}}}$, where E is the electric field across the film, ε_0 and ε_r are the absolute and relative dielectric constants and λ is an empirical constant[21]. Here we assume $E = V/d$ (d is the film thickness), which is a conservative estimate since we neglect the effect of surface charges and screening. Johnson's equation is used to model dielectric media[21] (see Supplementary Fig. S25a) with strongly interacting dipoles as indicated by the narrow peak of $\varepsilon_r(E)$.

2. **Clausius-Mosotti relation**: $\varepsilon_r(E) = \frac{N\mu}{\varepsilon_0 E}\left[cothb - \frac{1}{b}\right] + 1$, where N is the number of dipoles per unit volume and μ is the moment of individual dipoles. As shown in Supplementary Fig. S25b, our data cannot be fitted with this equation, used for non-interacting dipoles[22]. However, assuming clusters of dipoles the equation can be modified to $\varepsilon_r = \frac{N_{eff}\mu_{eff}}{\varepsilon_0 E}\left[cothb - \frac{1}{b}\right] + 1$ where N_{eff}= N/n_d and μ_{eff} = $n_d \times \mu$, where n_d defines the number of dipoles in each cluster. Assuming, n_d=240, our bias dependent permittivity data can be fitted well as shown in Supplementary Fig. S25c.

This clearly establishes the existence of interacting dipoles in our film.

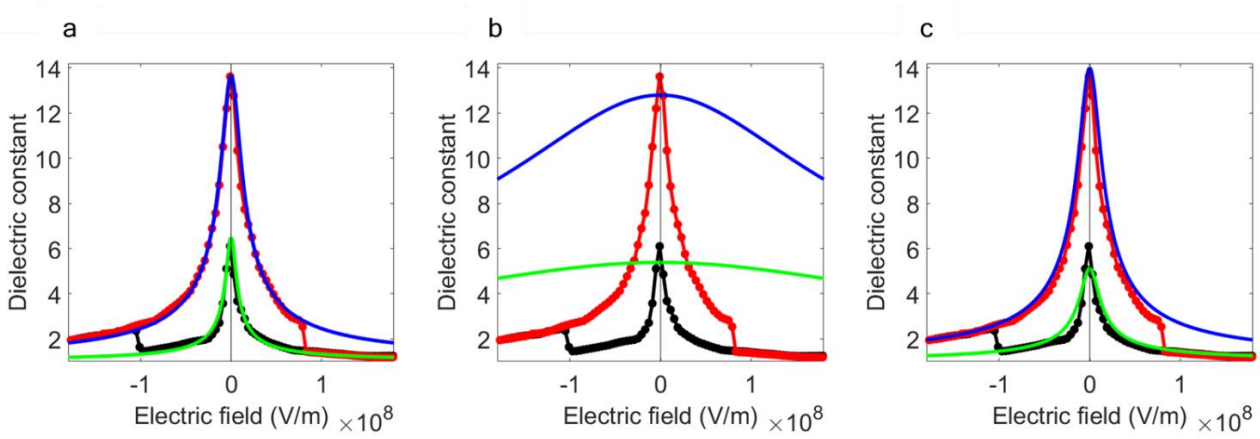

Supplementary Fig. S25 – (a) The relative permittivity fitted with Johnson's model. (b) The best fit for the measured permittivity data obtained from the Clausius-Mosotti relation. (c) The fitting obtained with the modified Clausius-Mosotti relation assuming formation of molecular clusters.

In all plots, red and black curves represent permittivity in forward (−8V to +8V) and reverse (+8V to −8V) voltage sweep in structure-A. The blue and green lines are fitted to the higher and lower permittivity states.

Section-S12: In-situ UV-Vis and Spectroelectrochemistry

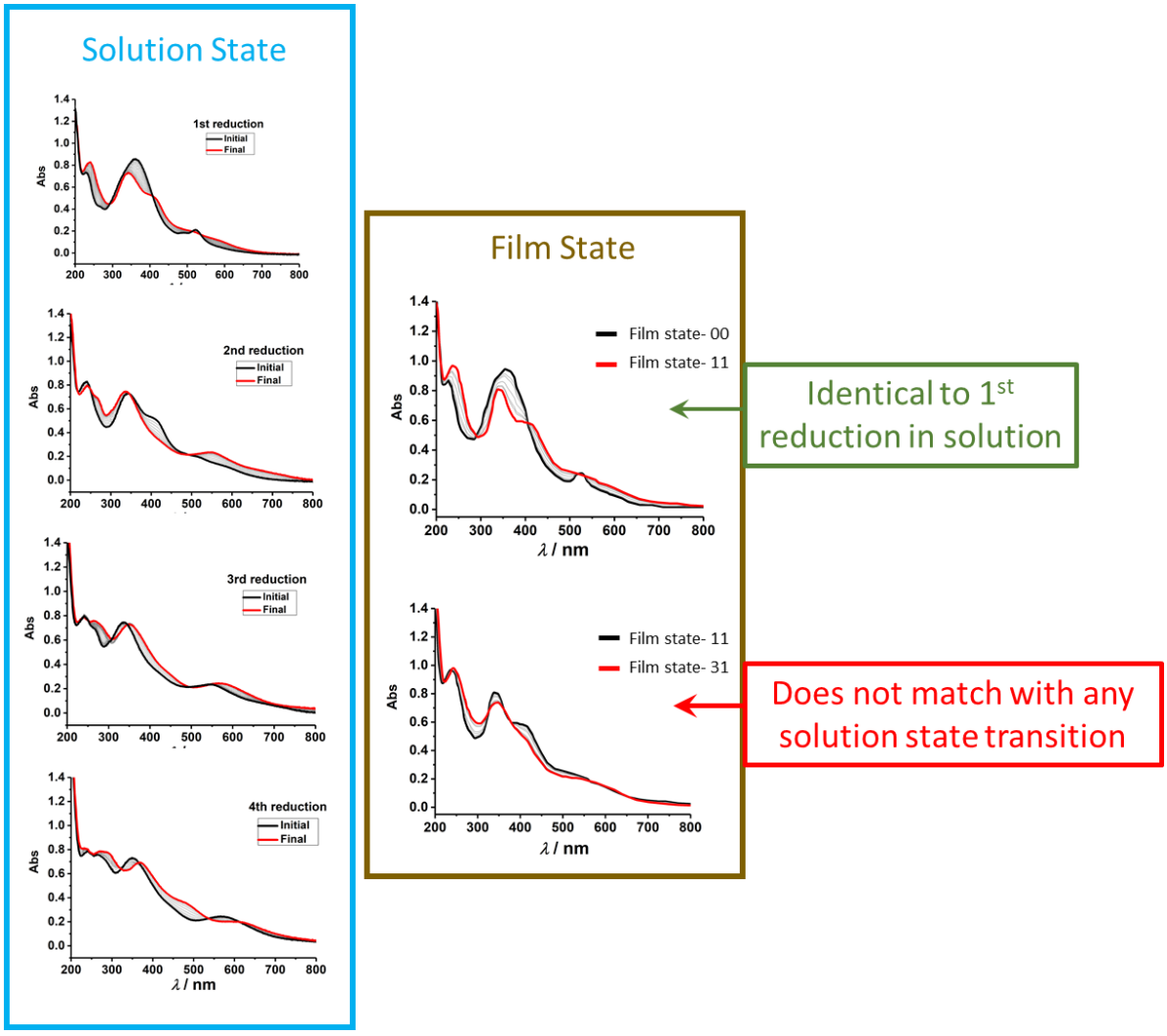

Supplementary Fig. S26 – Solution and film state spectroelectrochemistry data. Their correspondence reflects the quality/ purity of our material and the material handling skills involved.

Section-S13: In-situ Raman spectroscopy

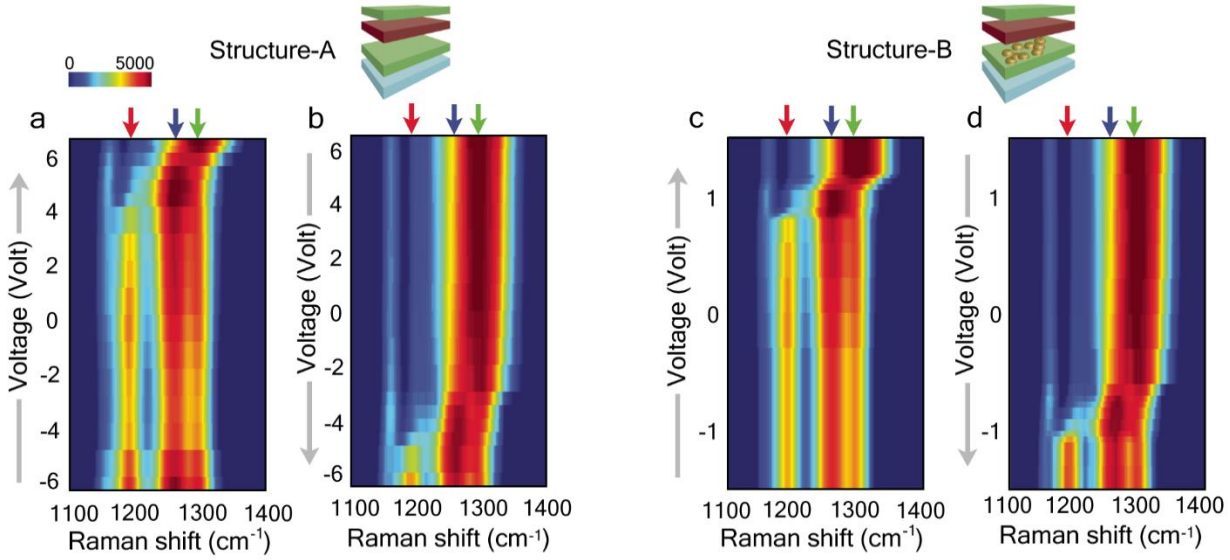

Supplementary Fig. S27 – (a-b) *Pseudo*-colour plot of the bias dependent Raman spectra measured on structure-A for forward and reverse voltage sweep.

(c-d) *Pseudo*-colour plot of the bias dependent the Raman spectra measured on structure-B for forward and reverse sweep.

The spectral changes observed in structure-B are very similar to structure-A indicating the same switching mechanism in both structures. In main Fig. 4, we show only the *in-situ* measurements on structure-A for simplicity.

Note – while performing the in-situ spectroscopy, we used a top ITO electrode. The *J(V)* of that device is shown in Extended Data Fig.7.

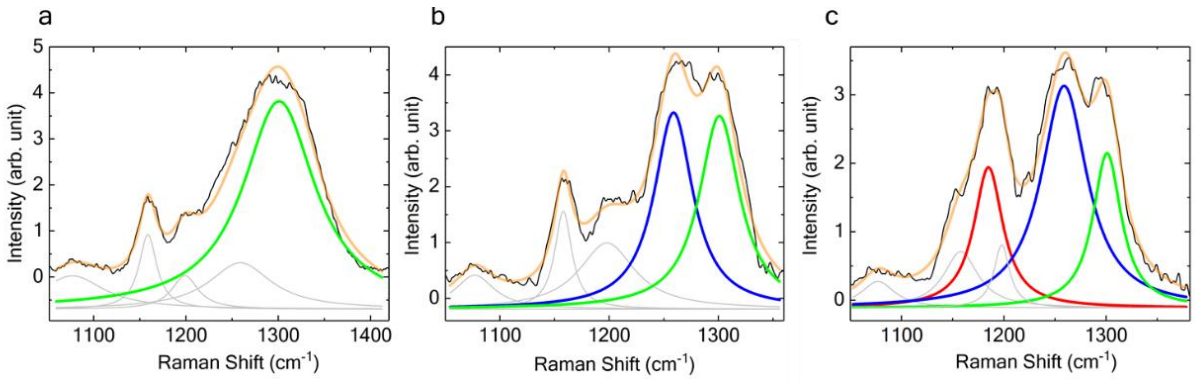

Supplementary Fig. S28 – (a) The Raman spectrum of $[RuL_2](PF_6)_2$ measured in the (00) state, corresponding to its original redox-state as isolated from solution. The dominant E_0 mode is fitted with a Lorentzian peak to determine its spectral weight.
(b) The Raman spectrum of the singly reduced state as measured in the (11) state. There are now two major Raman peaks visible. The E_0 and E_1 modes are fitted with Lorentz peaks to extract their respective spectral weights.
(c) The Raman spectrum of the (31) (CD) state. There are now three major Raman peaks observed, *i.e.*, E_0, E_1 and E_2 modes, which are fitted with three Lorentzians.

We observe only one Raman mode due to -N=N- in the non-reduced (di-cationic) state (00) of the molecule, *i.e.*, $[RuL_2]^{2+}$. Two azo-modes were observed in the singly reduced state (*i.e.*, state 11) and three modes in the doubly reduced CD-state (state 31).

1. In the non-reduced state all the azo-groups are in the same electronic state and so we observe only one mode in Raman. This is consistent with the X-ray structure of $[RuL_2](PF_6)_2$ where in the asymmetric unit, the matching d_{N-N}= 1.296(7)Å and 1.297(9)Å values justify the dominance of only one peak.

2. As shown in main Fig. 1b, for the singly reduced species (*i.e.* 1 1) the ∫-oriented azo pair (right diagonal) contributes more strongly to LUMO than the ʅ-oriented (left diagonal) azo pair, resulting in two Raman modes *viz.* E_0 and E_1.

3. While the ∫-oriented azo pair contributes more strongly to the LUMO, the LUMO+1 is dominated by the ʅ-oriented azo pair (Fig. 1b). This should lead to an expectation of a single Raman-mode in the doubly reduced state, characterized as (22). In our experiments,

we do not observe this molecular redox state. Instead we observe a total of three modes in the doubly reduced state. We observe pairs of modes E_0 and E_1 plus E_1 and E_2, which implies pairs of singly and triply reduced molecules, *i.e.* 50% (3) + 50% (1) => (31) *i.e.* the CD-state, as opposed to all-doubly reduced molecules.

Note-1:

Based on our *in-situ* measurements, we conclude that we observe a redox-driven switching and memory effect in our molecular device. Given a redox mechanism, electron injection from metal to the film is necessary which will mandate level alignment. However, so far as the memory effect and CD are concerned, there are two processes being operative:

1. Redox (*i.e.* charge injection)
2. Counterion displacement to create a coulombic asymmetry

While the redox only demands level alignment, the displacement of counterions is enabled by the electric field. So, the observed memristive phenomenon is an effect of both level alignment and field-driven ionic displacement.

Note-2:

While we observe a symmetry broken 31-state, we do not observe states like (21) or (10) due to the following reason:

Usually in a solid, there should be valence symmetry and only the (00), (11), (22) states should exist. (31) is an anomaly where this particular state is stabilized by counterion displacement causing a valence symmetry breaking. Notably, for every CD state there must be a corresponding symmetric state. For example, for (31) CD state, the symmetric state is (22) state. This automatically implies that every symmetric state must add up to be even numbers. If states like (21) and (10) were to exist, the corresponding symmetry states would have to be (1.5 1.5) and (0.5 0.5) implying fractional charge states which are impossible. Hence, states like (21) and (10) cannot exist. The only other state that could have existed is (20), produced by symmetry breaking of (11) state. DFT calculations show (11) is energetically favoured by 50 meV over (20). This preference is small but consistent to within ±5 meV across four datasets of complexes with four- and eight-molecule unit cells and either PF_6 or BF_4 counterions.

Section-S14: Hopping transport and origin of different conductance states

The electron transport in all three conductance states follows activated hopping and can be fitted with the Arrhenius equation yielding activation energies of 19, 29 and 54meV for on (00), intermediate (11) and off (31) state respectively (see Supplementary Fig. S29 a-c).

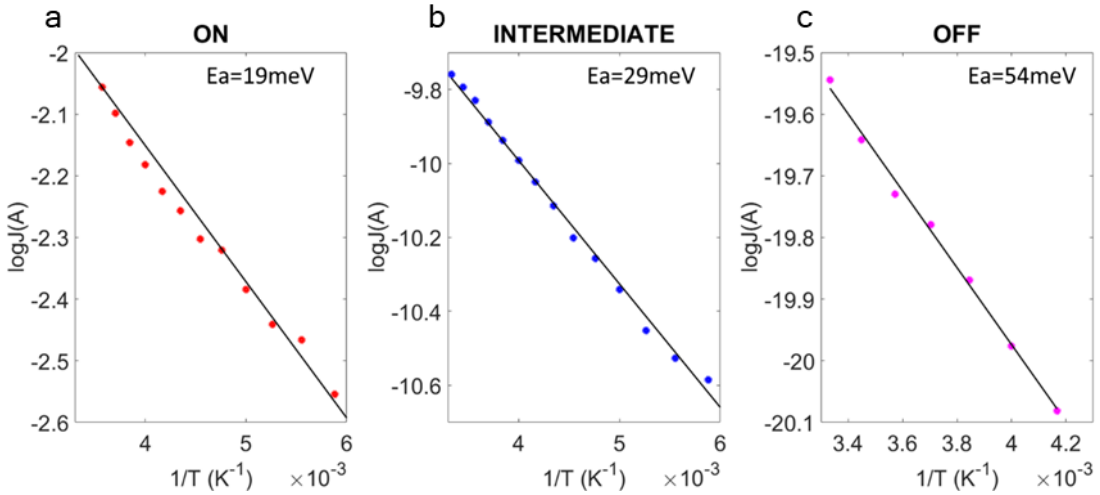

Supplementary Fig. S29 – Arrhenius Plot**:** activation energy of the (a) on (00), (b) intermediate (11) and (c) off state (31)

The hopping process involves the ligand centred LUMO+n orbitals that can be visualised by the schematic illustration, shown in Supplementary Fig. S30. Difference in the rate of intermolecular hopping in different redox states account for the difference in their conductance values. Note that according to Fermi's Golden Rule, the hopping rate is proportional to the acceptor density of states and the overlap integral between the donor and the acceptor molecular orbitals. Based on this, the following inferences can be drawn:

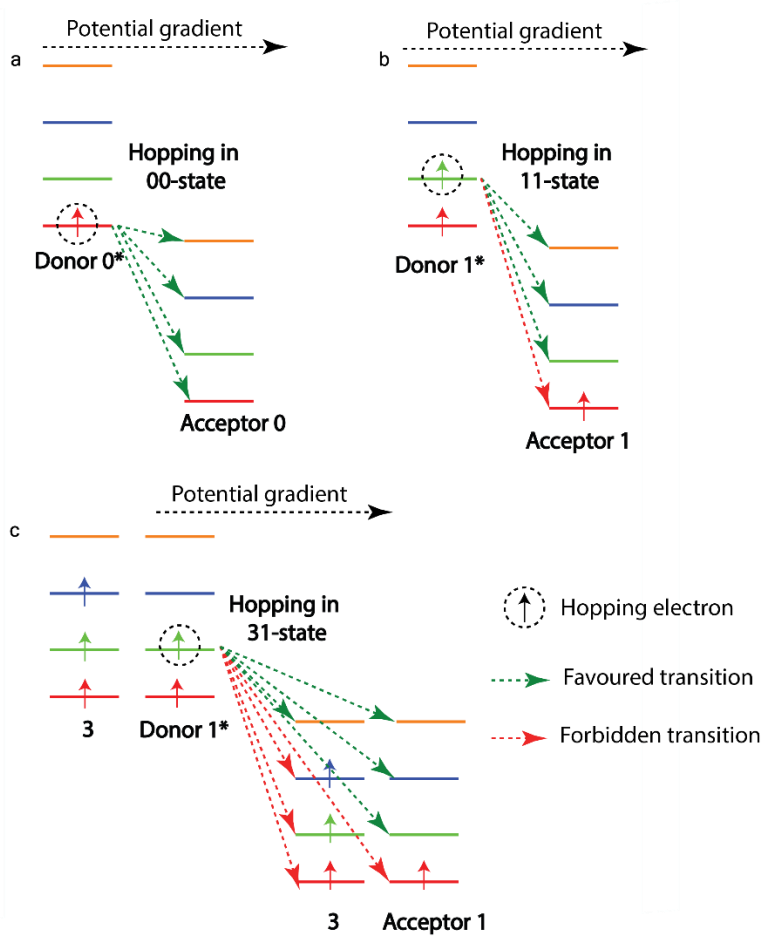

Supplementary Fig. S30 – Schematic illustration of electron hopping in different redox states, *viz.* (a) 00, (b) 11 and (c) 31. The red, green, blue and yellow levels represent LUMO, LUMO+1, LUMO+2 and LUMO+3 respectively (as defined in Fig. 1b). We use a transient donor species (denoted by *) along with an acceptor species to illustrate the idea. The electrons in dotted circles indicate hopping electrons. The green and red arrows indicate favoured and forbidden transitions.

a) State (00): In this state the donor molecule will have an electron in the antibonding which represents a transient state (denoted by a *) wherefrom the electron hops to an acceptor. The acceptor species for the (00) state is an unreduced molecule where the electron can hop into all 4 low-lying acceptor levels LUMO→LUMO+3 (indicated by the 4 green arrows).

b) State (11): For the (11) state, electron hopping to the occupied state will be prohibited (indicated by red arrow) and hence only three levels can accept the incoming electron.

Naturally, the number of acceptor orbitals in the (11) state is less than in the (00) state, and so is the hopping rate.

c) **State (31):** Owing to the high energy barrier induced by the high degree of electron accumulation, the triply reduced molecules are not likely to host a hopping electron. The difference between state (11) and (31) is, in (31) only half of the molecules will participate in hopping. Hence, the overlap integral between the hopping molecules will be significantly reduced from the (11) state and so (31) has the lowest conductance.

While the difference in hopping rate in a single hopping event is a small number, it gets accumulated following a power law across multiple hopping processes to yield the very large on/off ratio (Fig. 2b-d). For example, a factor of 1.8 times in hopping rate, accumulated over 12 hops yields an overall ratio > 10^3.

In addition, we have isolated the molecule in both the (00) state and (11) state. However, because there are 3 closely spaced molecular acceptor orbitals around -4eV, if we spin cast these complexes on ITO, the low ITO work function (~4.1eV) causes electron injection in the molecules and hence the isolated state is not retained. For example, putting (00) state on ITO yields (31)-CD state as explained in the main text. However, using a deep work function electrode like Pt, we can retain the isolated molecular state, at least in a short voltage span (±3V). So, spin casting films of comparable thickness (~35nm) in (00) and (11) state on Pt and Au electrode (spectroscopically verified), we measured their *J(V)* and show that they exactly overlap with our on-state and intermediate state providing a conclusive evidence of the proposed mechanism. In Supplementary Fig. S31 we show the measured current voltage characteristics of isolated (00) and (11) states for two different Pt/film/Pt device and one Au/film/Au device.

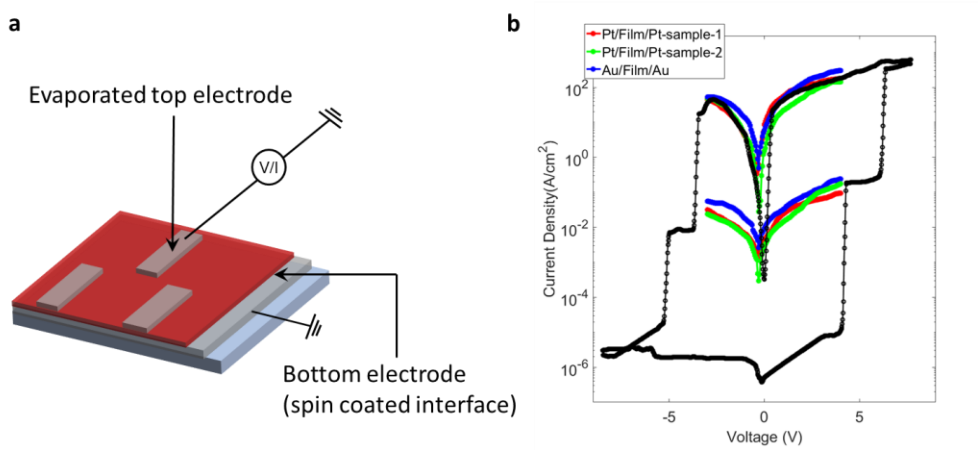

Supplementary Fig. S31 – (a) The device configuration used for the measurement. Designation of top and bottom electrodes: The electrode on which the film is spun on is denoted as the bottom electrode whereas the evaporated electrode is the top electrode. (b) The isolated (00) and (11) state characteristics in different electrode combinations and their close resemblance to the *J(V)* of structure-A. Two Pt/film/Pt devices (written as top electrode material/ film/ bottom electrode material) prepared in different batches were tested along with an Au/film/Au combination.

Note: Since we have a chain of molecules between the two electrodes, the film conductance is dominated by the intermolecular hopping rates and the electrode effect is not significant. Similar observations have been previously reported in long-chain molecular electronic devices[34,35].

Section-S15: Low T measurement

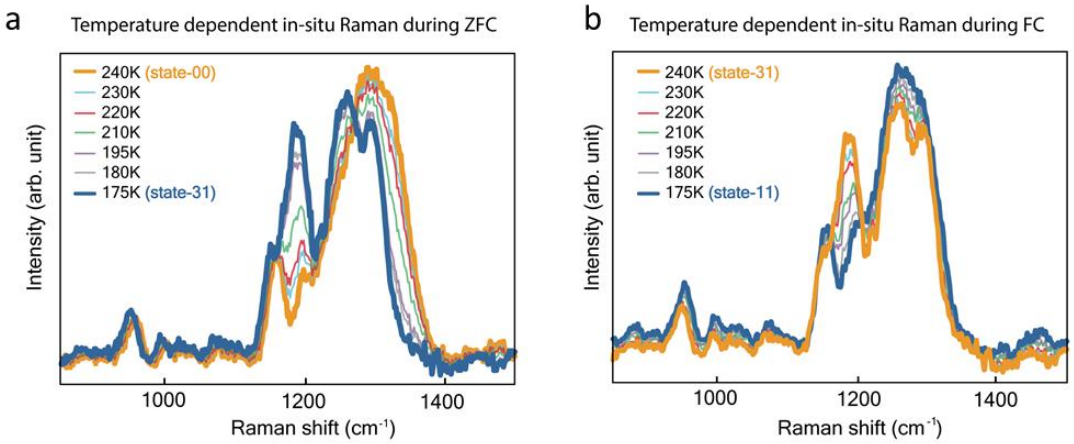

Supplementary Fig. S32 – (a) *In-situ* Raman spectra measured during ZFC at 2.5V while sweeping from 0V. Notably, at lower temperature values, the E_2 peak starts growing and by 175K the system gets frozen at 31 state supporting the *J(V)* shown in Fig. 5c. (b) *In-situ* Raman spectra measured at -3V during FC (while sweeping from +8V). Clearly at lower temperature values, the E_2 peak starts decaying below 240K and by 175K, (31) state is not formed at all supporting the *J(V)* shown in Fig. 5d.

Because of local variations in the film structure, the height and width of the barriers will vary a bit in a particular film, and so the temperature required for getting over the barrier also varies resulting in gradual transition observed both in FC and ZFC *J(V)* and Raman.

Definition of T_{CD}:

T_{CD} represents the minimum temperature required for the 'complete formation' of the CD (31) state. The 'complete formation' of the (31) state is deducted from *in-situ* Raman measurements, based on the intensity of the E_3 Raman mode. We defined T_{CD} as the temperature where the E_3 mode reaches 90% of its maximum value.

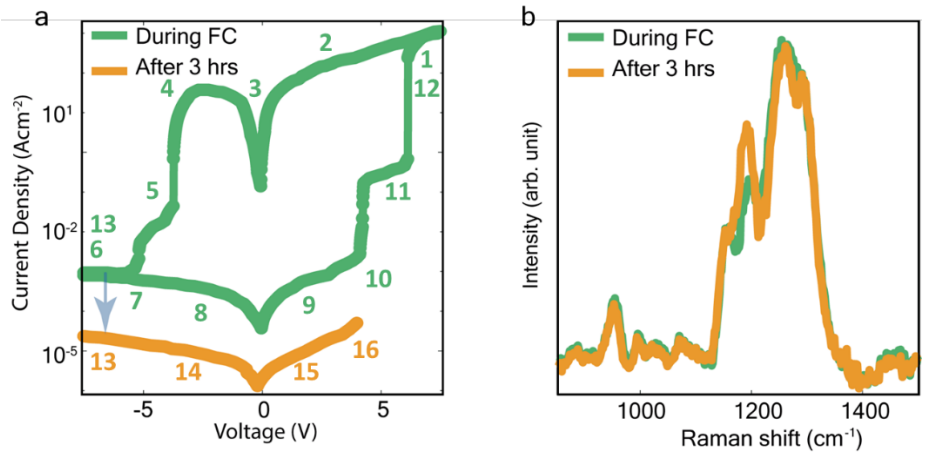

Supplementary Fig. S33 – (a) **Green** - *J(V)*, measured at 225K during FC (*i.e.*, voltage sweep starts at point-1, at ~ +7.5V). The FC scan can be followed by the 1-12 sequence. Point 13 in green curve shows an incompletely formed (31) state. **Yellow** - After the normal scan, a voltage of ~ -7V (point 13) was applied for 3 hours as a result of which the conductance decreased (13 in green to 13 in yellow) leading to a complete formation of the (31) state. Then the voltage was swept from 13-16 (in yellow).(b) *In-situ* Raman measured at -3V for the incompletely and completely formed 31 state corresponding to the green and yellow *I(V)* trace.

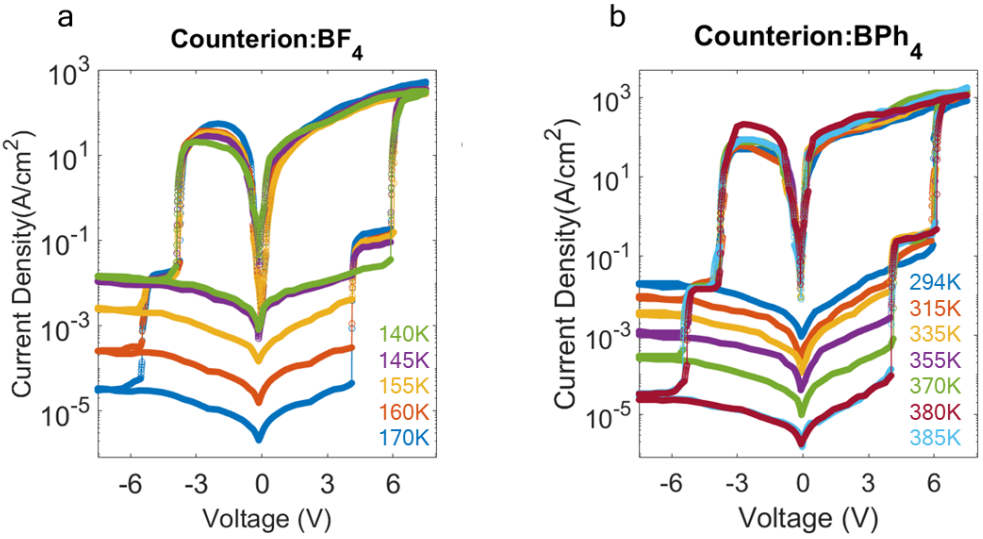

Supplementary Fig. S34: FC data for BF_4^- and BPh_4^-:

J(V.T)s (in FC) measured at different temperature for devices using counterions of different sizes.

Section-S16: Origin of hysteresis

Ion displacement is responsible for both hysteresis as well as CD but the ranges of counter ion (CI) displacements involved are different. CD involves a longer rage CI movement compared to that for the hysteresis (Note, both these rearrangement displacements of the counterions are on the sub-nm scale).

As shown in Supplementary Fig. S35a, at T<70 K the hysteresis gradually goes away. This implies that whereas a minimum activation energy of 20.5 meV is needed for the PF_6^- counterions to exhibit CD, only 6 meV is adequate to trigger their displacement for hysteresis (Supplementary Fig. S35b). Further, as shown in Supplementary Fig. S35b, the minimum energy required to enable complete hysteresis depends on the counterion size which further proves the role of counterion displacement in hysteresis.

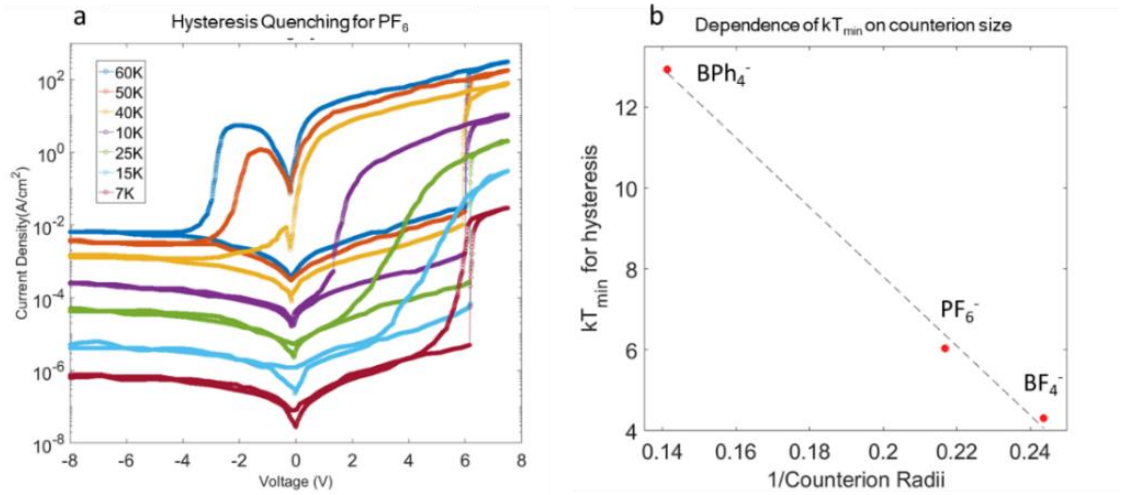

Supplementary Fig. S35 – (a) Quenching of hysteresis below 70K for the PF_6^- counterion case (note, below 170K, the CD state quenches resulting in a bi-stable *J(V)*). (b) Dependence of kT_{min} on counterion size where k is the Boltzmann constant and T_{min} is the minimum temperature required to exhibit a complete hysteresis.

Section- S17: Uniqueness of $[RuL_2]^{2+}$

The molecular system used in this article is unique, and is different in subtle but important ways from the one used in ref.[17]. While both are Ru^{II} complexes, the two ligands, *i.e.*, 2-phenylazopyridine – PAP (ref.[17]) and 2,6-bis(phenylazo)pyridine – L (this work) are dissimilar due to the following reasons:

(i) As shown in Supplementary Fig. S36a,b, PAP is a bidentate ligand whereas Lis a ***pincer*** ligand (coordinates as a tridentate ligand). Design of the ligand L may be visualized as follows: stitching of an phenyl-azo arm at the C(6) of the pyridine ring of PAP will produce the pincer ligand, L.

(ii) The redox events in the ruthenium complexes used both in ref. [17] and in this work are ligand-centric due to the presence of low-lying π*-acceptor orbitals of the azo-moieties. However, as shown in Supplementary Fig. S36 c, d, PAP can undergo two electron reductions, while L can take up four electrons. Thus, the maximum number of electron uptake in the two complexes $[Ru(PAP)_3]X_2$ (X= counter anion) and $[Ru(L)_2]X_2$ are six (3×2=6) and eight (2×4=8), respectively. The redox events in the two ligands are shown below:

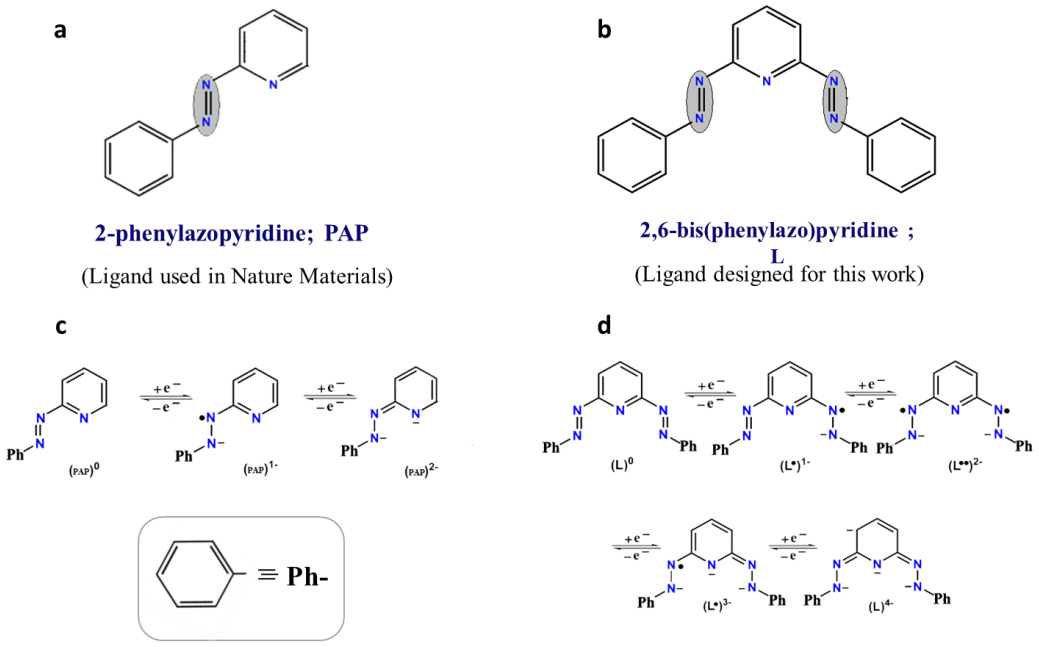

Supplementary Fig. S36 – (a, b) The structure of the two ligand systems PAP (used in ref.[17]) and L(this article). (c, d) The redox series of (c) PAPand (d) L.

(iii) The geometries of the coordinated azo-functions in two Ru-complexes are different, which may play a role in controlling the physical and chemical properties of the metal complexes. As shown in Supplementary Fig. S37, in $[Ru(PAP)_3]X_2$ three azo-functions (of three PAP) lie in three different planes while in $[Ru(L)_2]X_2$ two pairs of azo-functions (of two L) lie in two planes with each pair being co-planar.

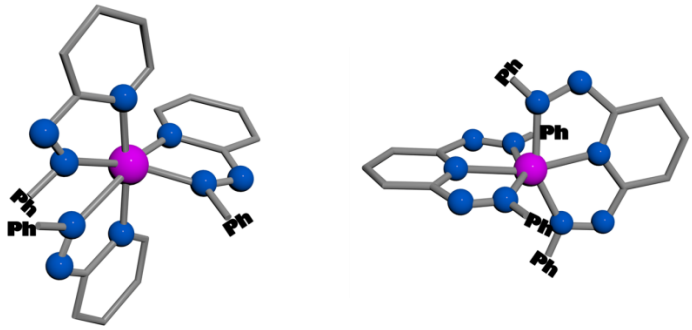

Supplementary Fig. S37 – The molecular structures of $[Ru(PAP)_3]X_2$ and $[Ru(L)_2]X_2$. In $[Ru(PAP)_3]X_2$, the three ligands are highly nonplanar whereas in $[Ru(L)_2]X_2$ the individual ligands are planar facilitating electron delocalization.

(iv) Due to the planarity of L, electron delocalization in $[Ru(L)_2]X_2$ is prominent while that in $[Ru(PAP)_3]X_2$ is insignificant. As calculated by DFT, in $[Ru(PAP)_3]X_2$, the redox electron density is delocalised across the azo-groups (see the LUMO, LUMO+1, LUMO+2 and LUMO+3 molecular orbitals in Fig. 1b), whereas in $[Ru(L)_2]X_2$, the electrons are localised on individual azo groups (LUMO, LUMO+1, LUMO+2, see Supplementary Fig. S38). The delocalised electron cloud in $[Ru(L)_2]X_2$ may result in a better intermolecular interaction facilitating CD exclusively in this molecular film and not in $[Ru(PAP)_3]X_2$.

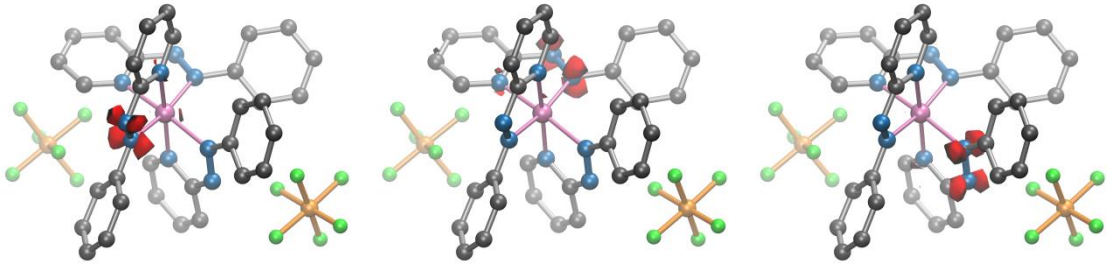

Supplementary Fig. S38 – Calculated low-lying electron-acceptor levels in $[Ru(PAP)_3](PF_6)_2$, calculated and plotted using the same method as for $[RuL_2](PF_6)_2$ (Fig. 1 b). MO surfaces are LUMO (left), LUMO+1 (middle) and LUMO+2 (right).

Chemical aspects of the complexes of PAP have been well explored over the past few decades. The knowledge developed with PAP ligand led to the design of a neutral pincer ligand L. Its transition metal complexes are being investigated over the last five years. The results reported so far[36,37,38,39] show great promise for their multiple-electron storage ability.

References:

1. Bandyopadhyay, A., Sahu, S., Higuchi, M. Tuning of nonvolatile bipolar memristive switching in Co (III) polymer with an extended azo aromatic ligand. *J. Am. Chem. Soc.* **133,** 1168-1171 (2011).

2. Hu, B. et al. Inorganic–organic hybrid polymer with multiple redox for high-density data storage. *Chem. Sci*. **5,** 3404-3408 (2014).

3. Lee, J. et al. Nitronyl Nitroxide Radicals as Organic Memory Elements with Both n-and p-Type Properties. *Angew. Chem. Int. Ed*. **50,** 4414-4418 (2011).

4. Seo, K., Konchenko, A. V., Lee, J., Bang, G. S., Lee, H. Molecular conductance switch-on of single ruthenium complex molecules. . *J. Am. Chem. Soc.* **130,** 2553-2559 (2008).

5. Nie, H.-J., Yao, C.-J., Sun, M.-J., Zhong, Y.-W., Yao, J. Ruthenium-bis-terpyridine complex with two redox-asymmetric amine substituents: potential-controlled reversal of the direction of charge-transfer. *Organometallics* **33,** 6223-6231 (2014).

6. Choudhury, S., Deb, A. K., Goswami, S. New ruthenium (II) complexes of α, α′-diimines. Synthesis, electrochemical and optical spectral properties of mononuclear complexes containing aryl (2-pyridylmethylene) amine and 2, 2′-bipyridine ligands. *J. Chem. Soc., Dalton Trans.***,** 1305-1310 (1994).

7. Tefashe, U. M., Nguyen, Q. V., Lafolet, F., Lacroix, J.-C., McCreery, R. L. Robust Bipolar Light Emission and Charge Transport in Symmetric Molecular Junctions. *J. Am. Chem. Soc.* **139,** 7436-7439 (2017).

8. Weil, J. A., Bolton, J. R. *Electron paramagnetic resonance: elementary theory and practical applications*. John Wiley & Sons, 2007.

9. Kaim, W. Mono-and binuclear tri-and tetracarbonyl complexes of chromium (0), molybdenum (0), and tungsten (0) with the 2, 2'-bipyrimidine radical anion. *Inorg. Chem.* **23,** 3365-3368 (1984).

10. Kaim, W. The transition metal coordination chemistry of anion radicals. *Coord. Chem. Rev.* **76,** 187-235 (1987).

11. Patra, S., Sarkar, B., Mobin, S. M., Kaim, W., Lahiri, G. K. Separating Innocence and Non-Innocence of Ligands and Metals in Complexes [(L) Ru (acac)$_2$]^n (n=− 1, 0,+ 1; L= o-Iminoquinone or o-Iminothioquinone). *Inorg. Chem.* **42,** 6469-6473 (2003).

12. Qi, Y., Desjardins, P., Meng, X., Wang, Z. Electrochromic ruthenium complex materials for optical attenuation. *Opt. Mater.* **21,** 255-263 (2003).

13. Kavan, L., Frank, O., Kalbáč, M., Dunsch, L. Supramolecular Assembly of Single-Walled Carbon Nanotubes with a Ruthenium (II)− Bipyridine Complex: An in Situ Raman Spectroelectrochemical Study. *J. Phys. Chem. C* **113,** 2611-2617 (2009).

14. Wang, S., Li, X., Xun, S., Wan, X., Wang, Z. Y. Near-infrared electrochromic and electroluminescent polymers containing pendant ruthenium complex groups. *Macromolecules*. **39,** 7502-7507 (2006).

15. Vickers, S. J., Ward, M. D. Facile preparation of a visible-and near-infrared-active electrochromic film by direct deposition of a ruthenium dioxolene complex on an ITO/glass surface. *Electrochem. Commun.* **7,** 389-393 (2005).

16. Li, X. et al. Spectroelectrochemical studies of hole percolation on functionalised nanocrystalline TiO 2 films: a comparison of two different ruthenium complexes. *PCCP* **13,** 1575-1584 (2011).

17. Goswami, S. et al. Robust resistive memory devices using solution-processable metal-coordinated azo aromatics. *Nat. Mater*. **16,** 1216 (2017).

18. Wang, X. F. et al. Interface Engineering with MoS_2–Pd Nanoparticles Hybrid Structure for a Low Voltage Resistive Switching Memory. *Small* **14,** 1702525 (2018).

19. Chen, P.-H. et al. Resistance switching characteristics induced by O2 plasma treatment of an indium tin oxide film for use as an insulator in resistive random access memory. *ACS Appl. Mater. Interfaces* **9,** 3149-3155 (2017).

20. Goswami, D. Y., Zhao, Y. *Proceedings of ISES World Congress 2007 (Vol. 1-Vol. 5): Solar Energy and Human Settlement*. Springer Science & Business Media, 2009.

21. Ang, C., Yu, Z. dc electric-field dependence of the dielectric constant in polar dielectrics: Multipolarization mechanism model. *Phys. Rev. B* **69,** 174109 (2004).

22. Talebian, E., Talebian, M. A general review on the derivation of Clausius–Mossotti relation. *Optik-International Journal for Light and Electron Optics*. **124,** 2324-2326 (2013).

23. Ganti, S. et al. Voltage Controlled Hot Carrier Injection Enables Ohmic Contacts Using Au Island Metal Films on Ge. *ACS Appl. Mater. Interfaces* **9,** 27357-27364 (2017).

24. Léonard, F., Talin, A. A. Electrical contacts to one-and two-dimensional nanomaterials. *Nat. Nanotechnol.* **6,** 773 (2011).

25. Padma, N., Betty, C. A., Samanta, S., Nigam, A. Tunable switching characteristics of low operating voltage organic bistable memory devices based on gold nanoparticles and copper phthalocyanine thin films. *J. Phys. Chem. C* **121,** 5768-5778 (2017).

26. Han, H., Kim, Y., Alexe, M., Hesse, D., Lee, W. Nanostructured ferroelectrics: fabrication and structure–property relations. *Adv. Mater.* **23,** 4599-4613 (2011).

27. Chua, L. If it's pinched it'sa memristor. *Semicond. Sci. Technol.* **29,** 104001 (2014).

28. Fan, F. et al. Conjugated polymer covalently modified graphene oxide quantum dots for ternary electronic memory devices. *Nanoscale* **9,** 10610-10618 (2017).

29. Miao, S. et al. Molecular length adjustment for organic azo-based nonvolatile ternary memory devices. *J. Mater. Chem.* **22,** 16582 (2012).

30. Chen, Y.-C. et al. Nonvolatile bio-memristor fabricated with egg albumen film. *Sci. Rep.* **5,** 10022 (2015).

31. Nguyen, V. C., Lee, P. S. Coexistence of Write Once Read Many Memory and Memristor in blend of Poly (3, 4-ethylenedioxythiophene): polystyrene sulfonate and Polyvinyl Alcohol. *Sci. Rep.* **6,** 38816 (2016).

32. Bessonov, A. A. et al. Layered memristive and memcapacitive switches for printable electronics. *Nat. Mater.* **14,** 199 (2015).

33. Wang, Z. et al. Capacitive neural network with neuro-transistors. *Nat. Commun.* **9,** 3208 (2018).

34. Yuan, L. et al. Controlling the direction of rectification in a molecular diode. *Nat. Commun*. **6,** 6324 (2015).

35. Livshits, G. I. et al. Long-range charge transport in single G-quadruplex DNA molecules. *Nat. Nanotechnol*. **9,** 1040 (2014).

36. Ghosh, P. et al. Introducing a New Azoaromatic Pincer Ligand. Isolation and characterization of redox events in its ferrous complexes. *lnorg. Chem.* **53,** 4678-4686 (2014).

37. Sengupta, D. et al. Exclusively ligand-mediated catalytic dehydrogenation of alcohols. *Inorg. Chem.* **55,** 9602-9610 (2016).

38. Pramanick, R., Bhattacharjee, R., Sengupta, D., Datta, A., Goswami, S. An Azoaromatic Ligand as Four Electron Four Proton Reservoir: Catalytic Dehydrogenation of Alcohols by Its Zinc (II) Complex. *Inorg. Chem.* **57,** 6816-6824 (2018).

39. Rath, S. P. et al. Effects of Ancillary Ligands on Redox and Chemical Properties of Ruthenium Coordinated Azoaromatic Pincer. *Inorg. Chem.* **57,** 11995-12009 (2018).